COULOMB CRYSTALS IN PLASMA PROCESSING REACTORS

BY

VIVEK VYAS

B.Tech., Indian Institute of Technology, Bombay, 2000

THESIS

Submitted in partial fulfillment of the requirements
for the degree of Master of Science in Electrical Engineering
in the Graduate College of the
University of Illinois at Urbana-Champaign, 2003

Urbana, Illinois

ABSTRACT

Dust particle transport in partially ionized plasmas has been the focus of many recent investigations as a consequence of concern over particle contamination of wafers during plasma processing of microelectronic devices and the use of particles to study nonideal plasmas. Under certain conditions (such as low power, low pressure, moderate gas flows, and high particle density) Coulomb interactions between the dust particles dominate over the kinetic processes and the particles arrange in ordered lattices known as "Coulomb crystals."

A self-consistent 3-D model for simulating dust particle transport in plasma processing reactors has been developed. A dust particle transport model has been integrated into a plasma equipment model to facilitate this study. The effect of varying the bias voltage of a capacitively coupled discharge, gas chemistries, particle diameter, and the number of particles on the propensity for Coulomb crystal formation was investigated. Higher ion drag forces at higher substrate biases produce voids in the plasma crystal. The presence of negative ions in the plasma closes the void in the plasma crystal. When the wake potential produced by ion streaming is included in the model, dust particles can form vertically correlated pairs when trapped in electric potential wells. Larger numbers of dust particles form multiple vertical layers when, in the absence of ion streaming, only a few, more populated, layers are formed. The acceleration due to ion-streaming is found to be significant only for larger particles.

ACKNOWLEDGMENTS

I would like to express my profound gratitude to my adviser, Prof. Mark J. Kushner, for his constant support, encouragement and valuable suggestions.

I would like to acknowledge the support of Sandia National Laboratories and the National Science Foundation (NSF). I am also thankful to Dr. Gregory A. Hebner for providing us with experimental data for comparison purposes and for insightful discussions.

I am also thankful to my fellow members in the Computational Optical and Discharge Physics Group: Rajesh Dorai, Arvind Sankaran, Pramod Subramonium, Kapil Rajaraman, Richard Moss, Alex Vasenkov, Ananth Bhoj, Shane Stafford, and Kelly Collier. Thanks also are due to my roommates and friends for making my stay in Urbana-Champaign such an enjoyable experience.

I am most indebted to my parents and relatives for their constant support and encouragement throughout the course of my education.

TABLE OF CONTENTS

1. INTRODUCTION

Dust particle transport in partially ionized plasmas has been the focus of many recent investigations as a consequence of concern over particle contamination of wafers during plasma processing of microelectronic devices and the use of particles to study nonideal plasmas.[1-5] Feature sizes of semiconductor devices are now approaching 0.1 μm sizes, whereas dust particulates are generated or often can grow to few microns in size in the reactor. Particles that land on wafers can then produce defects that lower device yield. The ability to predict the transport properties of these particles is therefore highly desirable in order to maximize the yield of processing.

Although modern clean rooms have removed sources of contamination external to the processing environment, the plasma itself may generate contaminating particles. Physical and chemical processes taking place in a plasma may form particles, generating a source of contamination greater than the external environment.[6-7] Particles can be sputtered off the electrodes, wafers and walls of the chamber. Particles may also be formed in the gas phase due to chemical processes.[8]

Particles were first observed in laboratory plasmas by Roth et al.[1] They observed dust particles near the plasma-sheath boundaries in a radio frequency discharge using laser light scattering methods. Later experiments by Selwyn et al.[6-7] and others demonstrated that particles could be found in dc and radio-frequency (RF) discharges in a variety of operating conditions (generally tens of milli-torr to a few torr, 0 to 500 V applied bias, and hundreds of watts and processing gas mixtures (eg. Ar, He/SiH_4). A typical experimental set-up used for these experiments is shown in Fig. 1.1.

Dust particles generally charge negatively to several hundreds to thousands of units of charge to balance electron and ion currents to the particles. The electrons are more mobile, which requires the particles to acquire negative potentials so that the sum of currents remains equal. A variety of forces act on the dust particle owing to its charge and mass. The various forces acting on a dust particle are depicted in Fig. 1.2. Sommerer et al.[9] and Barnes et al.[10] proposed that two forces dominate particle transport in the reactor: electrostatic and viscous ion drag. Electric fields accelerate the negatively charged particles in the opposite direction of the field, which usually produces dust motion towards the center of the reactor, or toward electric potential maxima.[7] Ions transfer momentum to the dust particles, which accelerates the particles in the direction of the net ion flux, typically towards the wall of the reactor. Dust particles accumulate in regions in the reactor where the net force acting on the particles is zero. Typically, the dust trapping sites are at the plasma-sheath boundaries adjacent to the electrodes, walls and other surfaces, where the ion drag and electrostatic forces balance.

Other forces also contribute to dust motion. Gravity can become an important force when the particle size exceeds a few microns. Gas temperature gradients produce thermophoresis, which accelerates particles away from heated surfaces and towards cooler regions. Fluid drag accelerates dust particles in the direction of the gas flow. As a result, high flow rates entrain particles in the feedstock gas flow, sweeping particles out of the reactor.

Reactor geometry greatly impacts trapping locations, as the forces on dust particles are sensitive to the structure of sheaths surrounding reactor surfaces. The disparity in electron and ion densities in the sheaths produces an electric field that

accelerates particles away from the surfaces thus balancing the opposing ion-drag force. The sheaths will "follow" the topography of grooves, notches, or raised elements, thereby modifying trapping locations and guiding particle motion. The electric fields within the sidewall sheaths will direct the particles toward the center of the groove.

Because the dust particles are generally charged, Coulomb interactions occur between the particles. Particle-particle interactions become particularly important if the dust density is high, such as within a trapping site. If the density of the particles reaches a critical level ($\cong 10^3$ cm^{-3}), the particles begin to display collective behavior as the Coulomb interactions between the particles dominate over the kinetic processes. Evidence of liquid and solidlike behavior in plasmas has been seen in a variety of laboratory discharges.[2-4] Under certain conditions such as low power, low pressure, and moderate gas flows, the dust particles become more ordered in the cloud and form lattices where the Brownian-type motion becomes insignificant. Such an ordered arrangement of dust particles is termed a "Coulomb solid" or a "plasma crystal." A 2-D plasma crystal under typical conditions (1.8 W, 110-mtorr, Ar plasma) is shown in Fig. 1.3. The plasma crystal moves as a collective unit or quasi-rigid body whose shape is relatively insensitive to most perturbations.

Several scaling laws have been derived from experimental observations of Coulomb solids. Melzer et al.[12] produced Coulomb crystals of 9.4 μm particles in RF discharges sustained in He. They found that reducing the gas pressure or increasing the discharge power resulted in melting of the crystal. These transitions were attributed to an increase in the effective temperature of the particles. The interparticle distance in the lattice increases with decreasing discharge power because the Debye shielding length is

smaller due to lower plasma density.[13] A larger separation is typically observed between larger particles due to a stronger repulsive force, since the amount of charge on the particle increases with its diameter.[3] Recently Hebner et al.[5] investigated particle-particle interactions directly from the lateral compression of 2-D plasma dust crystals confined in a parabolic potential well.

Dust particles have also been observed to arrange in vertically aligned structures or "strings" as shown in Fig. 1.4. Plasma ions flowing supersonically towards the negatively charged electrode or "ion streaming" generate wake fields behind the charged particle. The wake fields generated by the upper particles is found to influence the positions of lower particles. Recently Joyce et al.[15] developed a particle simulation that combines properties of molecular dynamics simulations for the short-range part of the shielded potential and with a particle-in-cell simulation for the long-range part. They observed particles forming hexagonal lattices when there is no ion streaming, and "strings" in the presence of streaming.

Experiments have demonstrated the formation of stable dust-free regions or "voids" in Coulomb crystals. Larger radial ion-drag forces at higher biases are responsible for the formation of a void as shown in Fig. 1.5. Samsonov and Goree[17] observed that the void has a sharp boundary with the surrounding dusty plasma and the electron density and ionization rate were enhanced in the void. This enhanced ionization rate leads to an electric field that is directed outward from the void's center. There is a balance of an inward electrostatic force and an outward ion drag force at equilibrium. Oscillations of charged dust particles trapped in a low temperature plasma sheath have also been observed, including vertical oscillations of single particles[18] as well as

horizontal dust lattice waves.[19] The study of these oscillations is a useful tool for evaluating the particle charge and particle-particle interaction potential.

In this study, we discuss a self-consistent three-dimensional model for simulating dust particle transport in plasma processing reactors. A dust particle transport model was self-consistently integrated into a plasma equipment model to facilitate this study. The plasma parameters in these reactors are obtained from the Hybrid Plasma Equipment Model (HPEM), developed at the University of Illinois.[20-21] The details of the HPEM are discussed in Chapter 2. The particle trajectories and trapping locations are obtained using the Dust Transport Module, which is discussed in Chapter 3. The characteristics of the Coulomb crystals in rf discharges are discussed in Chapter 4. The effect of varying the bias voltage of a capacitively coupled discharge, gas chemistries, particle diameter, and the number of particles on the propensity for crystal formation has been investigated. The effect of ion streaming on the morphology of Coulomb crystals is discussed in Chapter 5. A brief summary of this research is given in Chapter 6.

1.1 Figures

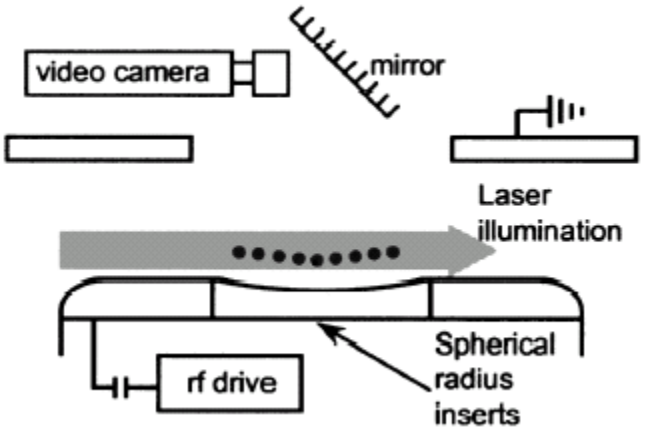

Fig. 1.1. A typical experimental set-up used to investigate Coulomb crystals in plasma processing reactors.[5] A spherical insert is used on the lower electrode to form an electrostatic trough in which the particles get trapped. The Coulomb crystal is illuminated using a laser beam. Time dependent trajectories of the particles are captured on videotape using a CCD camera and lens.

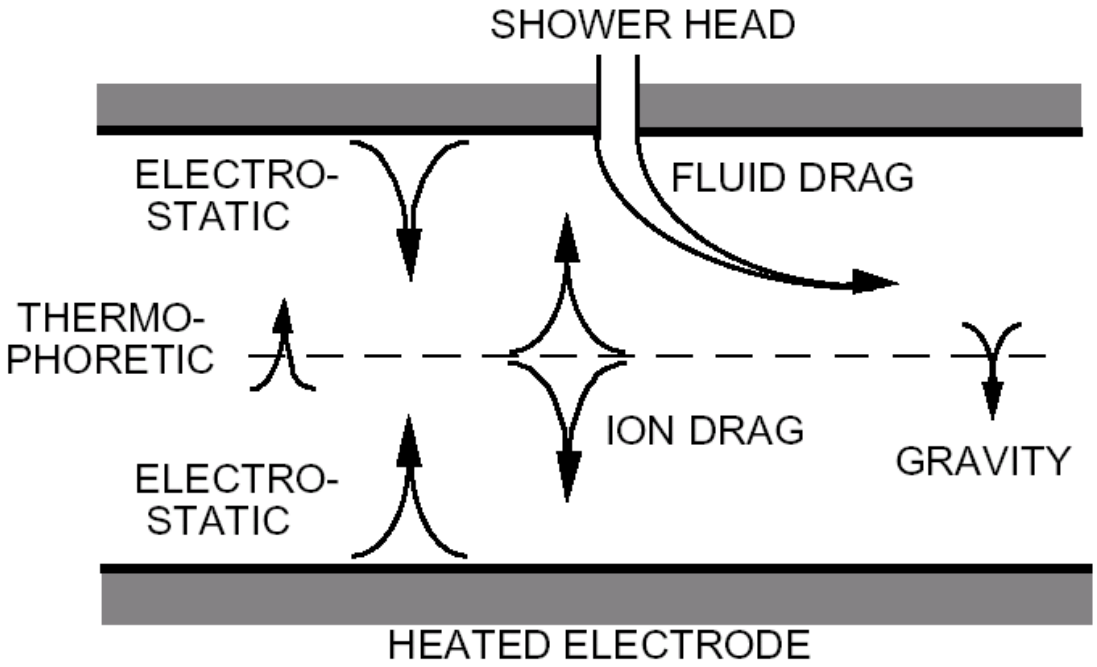

Fig. 1.2. Schematic of the forces acting on dust particles in plasmas.

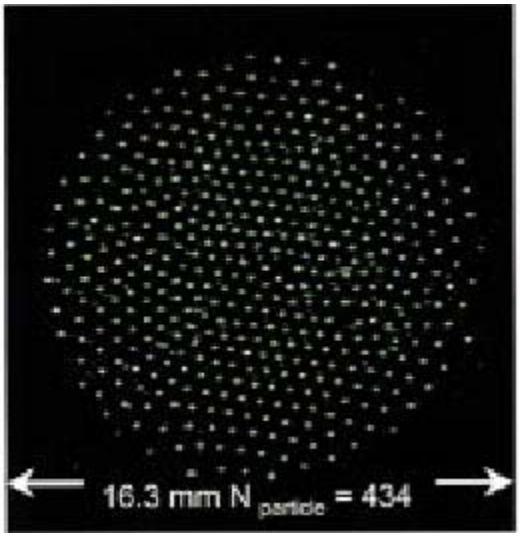

Fig. 1.3. Top view of optical light scattering from Coulomb crystal comprised of 434 8.3-μm diameter, melamine formaldehyde particles suspended in a 1.8 W, 110-mtorr argon plasma.[11]

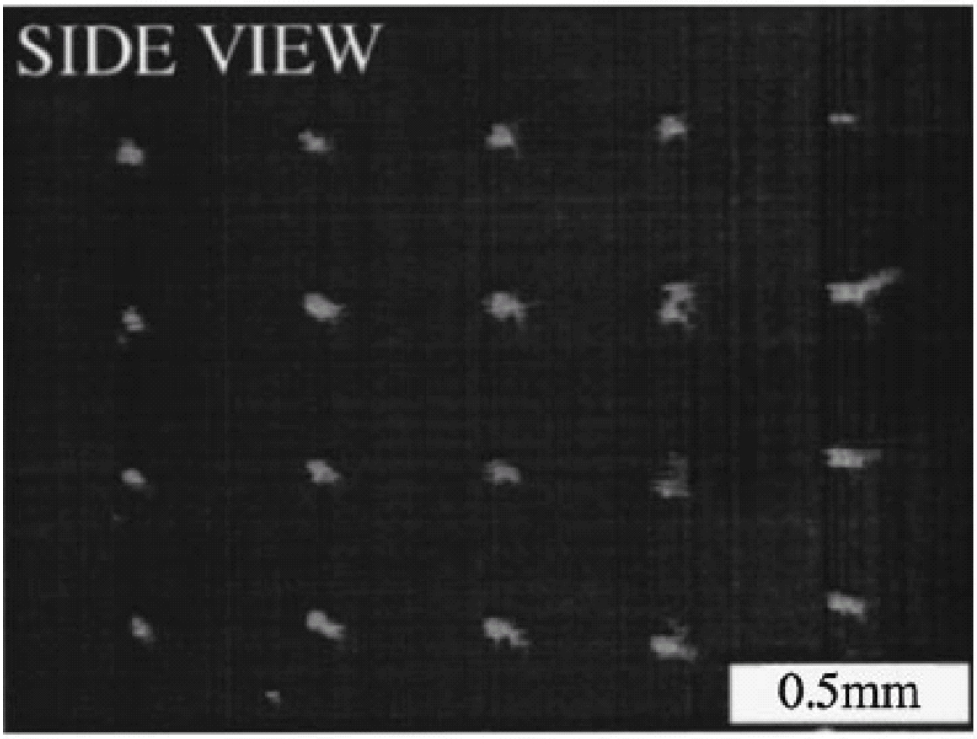

Fig. 1.4. Side view of the plasma crystal. Particles form "string-like" structures due to attractive ion-streaming force.[14]

(a)

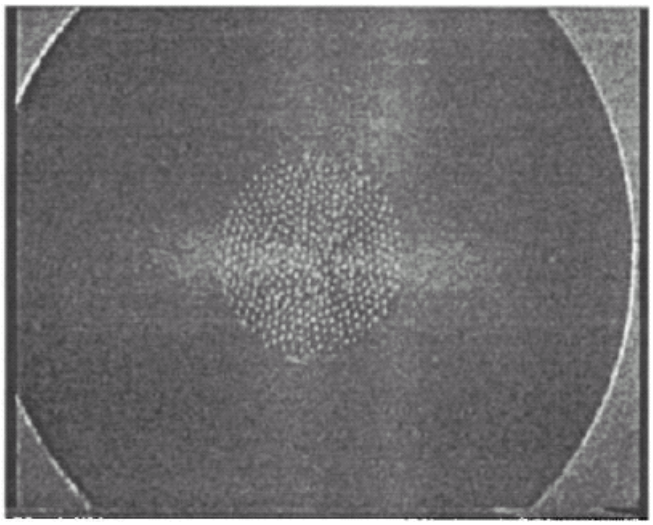

(b)

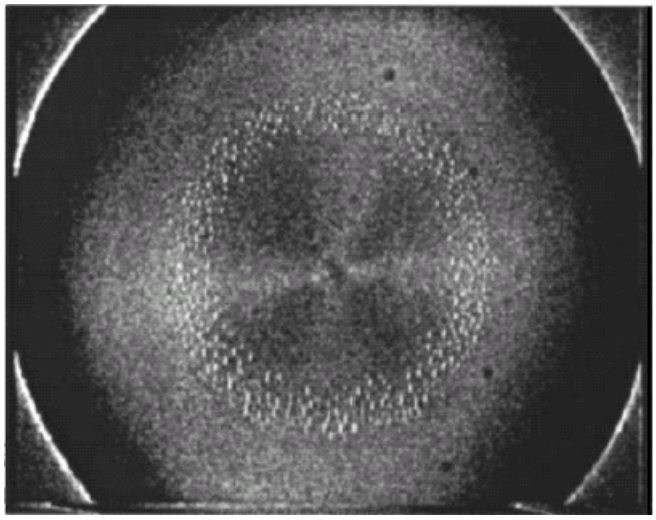

Fig. 1.5. Crystalline structure of 9.8 μm diameter dust particles trapped in an argon RF sheath at 0.13 mbar and 3 W power, and (b) centrally symmetric 7-mm-diameter void formed in the dust cloud in an argon RF sheath at 0.13 mbar and 10 W power.[16]

1.2 References

[1] R. M. Roth, K. G. Spears, G. D. Stein, and G. Wong, Appl. Phys. Lett. **46**, 253 (1985).

[2] L. Boufendi, A. Bouchoule, R. K. Porteous, J. Ph. Blondeau, A. Plain, and C. Laure, J. Appl. Phys. **73**, 2160 (1993).

[3] J. H. Chu, J. –B. Du, and I. Lin, J. Phys. D: Appl. Phys. **27**, 296 (1994).

[4] H. Thomas, G. E. Morfill, V. Demmel, J. Goree, B. Feuerbacher, and D. Möhlmann, Phys. Rev. Lett. **73**, 652 (1994).

[5] G. A. Hebner, M. E. Riley, D. S. Johnson, Pauline Ho and R. J. Buss, Phys. Rev. Lett. **87**, 235001 (2001).

[6] G. S. Selwyn, J. E. Heidenreich, and K. L. Haller, Appl. Phys. Lett. **57**, 1876 (1990).

[7] G. S. Selwyn, J. Singh, and R. S. Bennett, J. Vac. Sci. Technol. A **7**, 2758 (1989).

[8] S. L. Girshick, J. Chem. Phys. **94**, 826 (1991).

[9] T. J. Sommerer, M. S. Barnes, J. H. Keller, M. J. McCaughey, and M. J. Kushner, Appl. Phys. Lett. **59**, 638 (1991).

[10] M. S. Barnes, J. H. Keller, J. C. Forster, J. A. O'Neill, and D. K. Coultas, Phys. Rev. Lett. **68**, 313 (1992).

[11] G. A. Hebner, M. A. Riley, D. S. Johnson, P. Ho, and R. J. Buss, IEEE Trans.Plasma Sci. **30**, 94 (2002).

[12] A. Melzer, A. Homann and A. Piel, Phys. Rev. E **53**, 2757 (1996).

[13] J. B. Pieper, J. Goree, and R. A. Quinn, J. Vac. Sci. Technol. A **14**, 519 (1996).

[14] K. Takahashi, T. Oishi, K. Shimomai, Y. Hayashi, and S. Nishino, Phys. Rev. E **58**, 7805 (1998).

[15] G. Joyce, M. Lampe, and G. Ganguli, IEEE Trans. Plasma Science **29,** 238 (2001).

[16] R. P. Dahiya, G. V. Paeva, W. W. Stoffels, E. Stoffels, G. M. W. Kroesen, K. Avinash, and A. Bhattacharjee, Phys. Rev. Lett. **89**, 125001 (2002).

[17] D. Samsonov and J. Goree, Phys. Rev. E **59**, 1047 (1999).

[18] T. Nitter, T. K. Aslaksen, F. Melandsoî, and O. Havnes, IEEE Trans. Plasma Sci. **22**, 159 (1994).

[19] M. Zuzic, H. M. Thomas, and G. E. Morfill, J. Vac. Sci. Technol. A **14**, 496 (1996).

[20] W. Z. Collison and M. J. Kushner, Appl. Phys. Lett. **68**, 903 (1996).

[21] R. L. Kinder and M. J. Kushner, J. Vac. Sci. Tech. A **19**, 76 (2001).

2. HYBRID PLASMA EQUIPMENT MODEL

2.1 Introduction

The HPEM has been developed at the University of Illinois for simulating low-temperature, low-pressure plasma processes.[1-6] The HPEM addresses plasma physics and chemistry in a modular fashion. There is a series of modules captured in three main blocks: The Electromagnetics Module (EMM), the Electron Energy Transport Module (EETM), and the Fluid-Chemical Kinetics Module (FKM). Starting with an initial guess of plasma properties, the EMM computes the inductively coupled electric fields determined by inductive coils, and the magnetostatic fields induced by permanent magnets or dc current loops. These fields are then passed to the EETM. Together with a database describing electron collision cross sections, the EETM calculates electron kinetic properties such as electron energy distribution function, electron temperature, and electron impact rate coefficients. Results of the EETM are transferred to the FKM to determine plasma source and sink terms. The FKM solves the fluid continuity equations for species densities and plasma conductivity. Electrostatic fields are also derived in the FKM by either solving Poisson's equation or assuming quasi-neutrality. The outputs of the FKM are then fed back to the EMM and EETM modules. The whole process iterates until the results reach a preset convergence criterion. For an RF capacitively coupled plasma, as is the case in this work, only the EETM and FKM modules are used since there is no inductively coupled power source.

2.2 The Electromagnetics Module

The EMM computes time varying electric and magnetic fields for the HPEM. For an inductively coupled plasma, RF currents passing through the inductive coil generate azimuthal electric fields that are governed by Maxwell's equations. The EMM module calculates the spatially dependent azimuthal electric fields by solving Maxwell's equation under time harmonic conditions. Assuming azimuthal symmetry, Maxwell's equation for electric field is reduced to

$$-\nabla\cdot\frac{1}{\mu}\nabla E_{\varphi} = \omega^2\varepsilon E_{\varphi} - j\omega J_{\varphi} \tag{2.1}$$

where μ is the permeability, ε is the permittivity, ω is the driving frequency, and the current J_ϕ is the sum of the driving current J_o and the conduction current in the plasma. The conduction current is assumed to be of the form $J_\phi = \sigma E_\phi$. At pressures where the electrons are sufficiently collisional, the conductivity of the plasma is

$$\sigma = \frac{q_e^2 n_e}{m_e}\frac{1}{\nu_{me} + i\omega} \tag{2.2}$$

where q is the charge, n_e is the electron density, m is the mass, and ν_m is the momentum transfer collision frequency. The azimuthal electric field solution is determined by the iterative method of successive over relaxation (SOR). The weighting coefficient and the convergence criterion for the SOR are adjustable simulation parameters.

The static magnetic fields in the axial and radial directions are also determined in the EMM. Assuming azimuthal symmetry allows the magnetic field to be represented by a vector potential A with only an azimuthal component. A can be solved using

$$\nabla \times \frac{1}{\mu} \nabla \times A = j, \qquad B = \nabla \times A \tag{2.3}$$

where j is the source terms due to closed current loops at mesh points representing permanent magnets or dc coils. This equation is also solved using SOR.

2.3 The Electron Energy Transport Module

Free electrons are accelerated to high energies by the electric fields. These electrons then inelastically collide with neutrals, leading to neutral dissociation, excitation, and ionization. The electron impact reaction rates strongly depend on the electron temperature T_e, which is related to the electron energy distribution (EED) as

$$T_e = \frac{3}{2} \int f(\varepsilon)\, \varepsilon \, d\varepsilon \tag{2.4}$$

where ε represents electron energy and $f(\varepsilon)$ is the electron energy distribution. Inelastic collisions influence the EED by extracting energy from the electrons, resulting in a reduction of the high-energy tail of the EED. So for a collisional plasma, the EED does not behave as a Maxwellian. The EETM was designed to simulate these effects. There are two methods for determining these parameters. The first method determines the electron temperature by solving the electron energy conservation equation in the electron

energy equation module (EEEM). The second method uses a Monte Carlo Simulation to launch electron particles and collect statistics to generate the EEDF.

2.3.1 Electron energy equation method

For a plasma with weak interparticle collisions, the Boltzmann equation describes its kinetics:

$$\frac{\partial f_e}{\partial t} + v.\nabla_r f_e - \frac{e(E + v \times B)}{m_e}.\nabla_v f_e = \left(\frac{\delta f_e}{\delta t}\right)_{\text{collision}} \tag{2.5}$$

where $f_e = f_e(t,r,v)$ is the electron distribution function, ∇_r is the spatial gradient, ∇_v is the velocity gradient, m_e is the electron mass, and $\left(\frac{\delta f_e}{\delta t}\right)_{\text{collision}}$ represents the effect of collisions. The EEEM solves the zero-dimensional equation for a range of *E/N* (electric field divided by total gas density). The electron temperature and all its dependent quantities, like electron mobility and electron rate coefficients, are derived from the EED. This information is used in the solution of the electron energy equation

$$\nabla k \nabla T_e + \nabla \cdot (\Gamma T_e) = P_{\text{heating}} - P_{\text{loss}} \tag{2.6}$$

where k is the thermal conductivity, Γ is the electron flux determined by the FKM, T_e is the electron temperature, and P_{heating} is the power added due to conductive heating equal to $j \cdot E$. The current density and electric field are determined in the FKM. The electric field is the sum of the azimuthal field from the EMM and the radial and axial field found in the FKM. P_{loss} is the power loss due to collisions by the electrons.

2.3.2 Electron Monte Carlo simulation

The EMCS tracks the trajectories of electron pseudo particles in the electromagnetic fields obtained from the EMM module and the electrostatic fields obtained from the FKM. Statistics on electron energy distributions are gathered by tracking the particle motions and collisions. Initially the electrons are given a Maxwellian distribution and randomly distributed in the reactor weighted by the current electron density. Particle trajectories are computed using the Lorentz equation:

$$\frac{d\bar{v}}{dt} = \frac{q_e}{m_e}\left(\bar{E} + \bar{v} \times \bar{B}\right) \tag{2.7}$$

where $\bar{v}$, $\bar{E}$, and $\bar{B}$ are the electron velocity, local electric field, and magnetic field, respectively. Equation (2.7) is updated using a second order predictor corrector method. The electron energy range is divided into discrete energy bins. Within an energy bin, the collision frequency, ν_i, is computed by summing all the possible collisions within the energy range,

$$\nu_i = \left(\frac{2\varepsilon_i}{m_e}\right)^{\frac{1}{2}} \sum_{j,k} \sigma_{ijk} N_j \tag{2.8}$$

where ε_i is the average energy within the bin, σ_{ijk} is the cross section at energy i for species j and collision process k, and N_j is the number density of species j. The free-flight time is randomly determined from the maximum collision frequency. After the free flight, the type of collision is determined by the energy of the pseudoparticle. The

corresponding energy bin in referenced and a collision is randomly selected from that energy bin, with a null reaction making up the difference between the maximum and actual collision frequency. Finally, the electron temperature, collision frequency and electron impact rate coefficients are evaluated based on EEDs with the process cross section at the specified location.

2.4 The Fluid-Chemical Kinetics Module

In the FKM, fluid equations, together with chemical reactions, are solved to obtain plasma species, densities and fluxes. The FKM also computes electrostatic fields by either solving Poisson's equation or using an ambipolar field approximation.

The continuity equation that describes the density evolution rate for any species is

$$\frac{\partial N_i}{\partial t} = -\nabla \cdot \Gamma_i + S_i \tag{2.9}$$

where N_i, Γ_i, and S_i are the species density, flux, and source for species i. The flux for each species can be determined by using a drift diffusion or a heavy body momentum equation. Electron densities are determined using the drift diffusion formulation,

$$\Gamma_i = \mu_i q_i N_i \overline{E}_s - D_i \nabla N_i \tag{2.10}$$

where μ_i is the mobility of species i, D_i is the diffusion coefficient, q_i is the species charge in units of elementary charge, and E_s is the electrostatic field. Heavy ion and neutral fluxes can be determined by using the previous drift diffusion method or by using the heavy body momentum equation:

$$\frac{\partial \Gamma_i}{\partial t} = -\frac{1}{m_i}\nabla(N_i k T_i) - \nabla\cdot(N_i \bar{v}_i \bar{v}_i) + \frac{q_i}{m_i} N_i \bar{E} - \sum_j \frac{m_j}{m_i + m_j} N_i N_j (\bar{v}_i - \bar{v}_j) \nu_{ij} \qquad (2.11)$$

where T_i is the species temperature, $\bar{v}_i$ is the species velocity given by Γ_i / N_i, and ν_{ij} is the collision frequency between species i and species j.

The gas and ion temperatures are determined from the energy equation for each species:

$$\frac{\partial N_i c_v T_i}{\partial t} = \nabla\cdot\kappa_i \nabla T_i - P_i \nabla\cdot\vec{v}_i - \nabla\cdot(\vec{\varphi}_i \varepsilon_i) + \frac{N_i q_i^2}{m_i \nu_i} E_s^2 + \frac{N_i q_i^2 \nu_i}{m_i(\nu_i^2 + \omega^2)} E^2$$
$$+ \sum_j 3\frac{m_{ij}}{m_i + m_j} N_i N_j R_{ij} k (T_j - T_i) \qquad (2.12)$$

where N_i is the density of species i, c_v is specific heat, T_i is the species temperature, κ_i is the thermal conductivity of species i, P_i is the partial pressure of species i, $\vec{v}_i$ is the species velocity, $\vec{\varphi}_i$ is the flux of species i, ε_i is the internal energy of species i, E_s is the electrostatic field, E is the RF field, m_i is the mass of species i, m_{ij} is the reduced mass, ν_i is the momentum transfer collision frequency for species i, and R_{ij} is the collision frequency for the collision process between species i and j.

In the FKM, the process of solving the continuity equation is coupled with the derivation of electrostatic fields. These fields determine the drift flux terms used in the continuity equation. There are two alternative ways for the FKM to calculate the

electrostatic fields. The first option is to directly solve Poisson's equation. The time evolving electrostatic potential is related to the net charge density as

$$\nabla.\varepsilon\nabla\Phi = -\rho \tag{2.13}$$

where ε is the permittivity, Φ is the electrostatic potential, and ρ is the net charge density. The charge density is numerically estimated using a first-order Taylor series expansion:

$$\rho^{t+\Delta t} = \rho^{t} + \Delta t.\frac{\partial\rho}{\partial t}\bigg|^{t+\Delta t} \tag{2.14}$$

where ρ^{t} is the charge density at time t and $\rho^{t+\Delta t}$ is the charge density at time $t+\Delta t$. The evolution rate of the charge density $\frac{\partial\rho}{\partial t}$ is determined by the gradient of the total current density j:

$$\frac{\partial\rho}{\partial t} = -\nabla.j + S \tag{2.15}$$

where S is the source function of charges. In the plasma region, $j = \sum_i q_i(-D_i\nabla n_i + q_i(-\nabla\Phi))$ in materials, $j = \sigma(-\nabla\Phi)$ where σ is the material conductivity.

The second option is to compute electrostatic fields using a quasi-neutrality approximation over the entire plasma region. Under such an assumption, the electron

density is equal to the total ion charge density at all locations. At steady state, this requires that

$$-\nabla.\Gamma_e + S_e = \sum_i q_i(-\nabla.\Gamma_i + S_i) \tag{2.16}$$

or

$$\nabla.(\mu_e n_e \nabla\Phi + D_e \nabla n_e) + S_e = \sum_i q_i(\nabla.(-\mu_i n_i \nabla\Phi + D_i \nabla n_i) + S_i) \tag{2.17}$$

when using drift-diffusion equations for both electrons and ions. S_e and S_i represent electron and ion source functions, respectively.

The plasma parameters obtained from the HPEM (such as species densities, electrostatic potentials and fluxes) are then used in the Dust Transport Module to compute dust particle trajectories and trapping locations. Details of the DTM are discussed in the following chapter.

2.5 References

[1] P. L. G. Ventzek, R. J. Hoekstra, and M. J. Kushner, J. Vac. Sci. Technol. B **12**, 416 (1993).

[2] P. L. G. Ventzek, M. Grapperhaus, and M. J. Kushner, J. Vac. Sci. Technol. B **16**, 3118 (1994).

[3] W. Z. Collison and M. J. Kushner, Appl. Phys. Lett. **68**, 903 (1996).

[4] M. J. Kushner, W. Z. Collison, M. J. Grapperhaus, J. P. Holland, and M. S. Barnes, J. Appl. Phys. **80**, 1337 (1996).

[5] M. J. Grapperhaus and M. J. Kushner, J. Appl. Phys. **81**, 569 (1997).

[6] S. Rauf and M. J. Kushner, J. Appl. Phys. **81**, 5966 (1997).

3. DUST TRANSPORT MODULE

The Dust Transport Module (DTM) is a 3-D module in which the trajectories of dust particles are integrated based on mechanical and electrical forces. The integrated dust transport module is based on a 2-D dust transport model previously developed at the University of Illinois.[1] The forces included in the model are ion drag, fluid drag, electrostatic, thermophoretic, coulomb, self-diffusive, gravity and Brownian motion. The details of the module are described in the following sections.

3.1 Particle Charge

In order to determine the charge on the particle, the particle's potential must be calculated. In the DTM, the particle's potential is based on the electron and ion currents to the particle, which are functions of the position (*r,z*) and the particle radius *a*. The ion flux to the particle is given by the orbital motion limited (OML) current, which depends on the plasma density and the ion energy. The ion and electron currents to a particle are

$$I_I = \pi\ a^2 N_I\ q\sqrt{\frac{2E_I}{m_I}}\left(1-\frac{q\Phi}{E_I}\right) \tag{3.1}$$

$$I_e = \pi\ a^2 N_e\ q\sqrt{\frac{8kT_e}{\pi m_e}}\ \exp\left(\frac{q\Phi}{kT_e}\right) \tag{3.2}$$

where a is the particle radius, T_e is the electron temperature, m_e is the electron mass, m_I is the ion mass, E_I is the ion energy, N_e is the electron density, N_I is the ion density, and Φ is the particle potential. The particle electrical floating potential is obtained by requiring

that the negative and positive currents to the particle are equal. The charge on the particle Q ultimately is given by[2,3]

$$Q = C\,\Phi\,,\; C = 4\pi\,\varepsilon_o a\left(1+\frac{a}{\lambda_L}\right) \tag{3.3}$$

where C is the capacitance of the dust particle and λ_L is the linearized Debye length. This is merely the capacitance of two concentric spheres with a separation distance of λ_L. The shielding length of the plasma from the highly charged particle by ions and electrons is obtained by linearizing the Poisson-Vlassov equation[2]:

$$\frac{1}{\lambda_L} = \sqrt{\frac{e^2}{\varepsilon_o}\left(\frac{N_e}{kT_e}+\frac{N_I}{2E_I}\right)} \tag{3.4}$$

3.2 Ion Drag Force

Ions exchange momentum with dust particles by performing hyperbolic orbiting around them or by direct collisions. These orbital and real collisions essentially accelerate dust in the direction of the net ion motion. The ion-dust momentum transfer cross-section is calculated according to the semi-analytic formula by Kilgore et al.[3]

$$\sigma = b^2\,c_1\,\ln\left(1+\frac{c_2}{(b/\lambda_L)^2}\right),\; b = \frac{Q^2}{4\pi\,\varepsilon_0 E_I} \tag{3.5}$$

where c_1 = 0.9369 and c_2 = 61.32 are semi-empirical values. Recently Khrapak et al.[4] have derived an expression for the ion drag force from first principles, which agrees well with the numerical calculations of Kilgore et al.[3] A molecular dynamics simulation of ion-dust particle interaction yields essentially the same cross section,[5] and so the computationally less expensive method of Eq. (3.5) is used.

3.3 Fluid Drag Force

Assuming that the particles are rigid spheres, the particles may either become entrained in the neutral gas flow or decelerate due to the viscosity of the gas, depending on the relative velocities of the particles and the gas. The fluid drag force has two factors for non-Stokesian flow, utilizing $C_D(Re)Re/24$ as the correction due to inertial effects and $C\,(Kn)$ for the slip correction factor.[6-7]

$$C_D(\,Re\,)\frac{Re}{24} = 1 + 0.173\,Re^{0.657} + \frac{0.01721\,Re}{1 + 16300\,Re^{-1.09}} \tag{3.6}$$

$$C(Kn) = 1 + Kn\left(\alpha + \beta \exp(-\frac{\gamma}{Kn})\right) \tag{3.7}$$

The Reynolds number for particles is defined by $Re = \rho\, d \left|\vec{v}_i - \vec{u}\right| / \mu$, where ρ is the gas density. As Re is usually less than 10 for most conditions, the inertial correction factor is nearly equal to unity.

3.4 Thermophoresis

Thermophoresis arises due to temperature gradients in the neutral gas. On the average, gas molecules with higher temperatures will exchange more energy in momentum transfer collisions with dust particles than will the colder gas molecules.

This has the effect of pushing particles in the direction toward cooler regions of gas or away from heated surfaces. The thermophoretic force used in the DTM has K_T as the slip correction factor on the particle as developed by Talbot et al.,[6] which depends on the Knudsen number *Kn* of the dust particle.

$$K_T = \frac{2C_s\left(\frac{k_g}{k_p} + C_t Kn\right)}{\left(1 + 3C_m Kn\right).\left(1 + 2\frac{k_g}{k_p} + 2C_t Kn\right)} \tag{3.8}$$

where k_g and k_p are the gas and particle thermal conductivities; C_t, C_s, and C_m are the thermal creep coefficient, temperature jump coefficient, and velocity jump coefficient, respectively. *Kn* is the ratio of the gas mean free path to the particle radius; $k_g = (15/4)\,\mu R/M$ for polyatomic gases, where *R* is the ideal gas constant; and *M* is the gas molecular weight.

3.5 Coulomb Force

The Coulomb repulsive force between particles is based on the particle's shielded plasma potential, using the Debye-Huckel form[2]

$$\Phi(r) = \Phi_0 \ \frac{a}{r} \ \exp\left(-\frac{(r-a)}{\lambda_L}\right) \tag{3.9}$$

The interparticle Coulomb force between particles at locations $\vec{r}_1$ *and* $\vec{r}_2$, separated by distance $R = |\vec{r}_1 - \vec{r}_2|$ is then

$$\vec{F}\left(\vec{r}_1, \vec{r}_2\right) = \frac{Q_1 Q_2}{4\pi\varepsilon_o} \frac{1}{R}\left(\frac{1}{R} + \frac{1}{\lambda_L}\right) \exp\left(-\frac{R - \left(\frac{a_1 + a_2}{2}\right)}{\lambda_L}\right) \frac{\vec{r}}{R} \qquad (3.10)$$

Trajectories of dust particles under the influence of these forces are simultaneously integrated using a second-order Runge-Kutta technique. When considering interparticle forces, the calculation time required to account for the interaction of all pairs of pseudoparticles scales as N^2 (where N is the number of pseudoparticles), which can lead to lengthy computational times when thousands of pseudoparticles are used in the DTM. For computational speedup, interparticle forces are included only if the particles are within a specified distance of each other. This distance was determined by parameterizing the model. There is little qualitative difference in the results for interacting distances greater than $3\lambda_L$. Hence the maximum interaction distance was set to $5\lambda_L$ in order to include sufficient interactions with particles while avoiding unnecessarily large computational times.

Dust particles also undergo Brownian motion. However, unless the particle size is very small, Brownian motion is expected to be insignificant compared to ion-drag, fluid-drag, and electrostatic forces. Self-diffusive force, which basically accounts for the diffusion of dust particles moving in a concentration gradient, is also included in the model. The net force is then

$$\vec{F}(\vec{r}) = M_i \vec{g} \text{ (gravity)} + Q_i \vec{E}_i \text{ (electrostatic)} + \sum_{\text{ions}} \sigma(\varepsilon_i)\, \Phi(\vec{r},\vec{v}_I)\, s_I \text{ (ion - drag)}$$

$$- 6\pi\mu r_i v K_T \frac{\nabla T}{T} \text{ (thermophoretic)} - \frac{6\pi\mu r_i}{C(Kn)} (\vec{v}_i - \vec{u})\, C_D(Re)\frac{Re}{24} \text{ (fluid - drag)}$$

$$- kT_i \frac{\nabla N_i}{N_i} \text{ (self - diffusion)} + \frac{M_{gas}\langle v\rangle}{\Delta t} \sqrt{\frac{\pi N_{gas}\langle v\rangle \Delta t\, d_i^2}{4}} \text{ (Brownian)}$$

$$+ \frac{Q_i}{4\pi\varepsilon_o} \sum_j \frac{Q_j}{R_{ij}} \left(\frac{1}{R_{ij}} + \frac{1}{\lambda_L}\right) exp\left(-\frac{R_{ij} - a}{\lambda_L}\right) \vec{r} \text{ (Coulomb)} \qquad (3.11)$$

3.6 Coupling of HPEM and DTM

The integrated dust transport module and the plasma kinetics models are based on the previously described HPEM[8-9] and the DTM.[1] When used separately, the HPEM produces plasma parameters (ion and neutral fluxes; electron, ion and neutral temperatures; and electric fields) which are used, in a postprocessing manner, in the DTM to calculate forces on the dust particles and their trajectories. As a result of the postprocessing nature of the DTM, feedback to the plasma resulting from the charge and the surface chemistry of the particles was not previously included. That inconsistency is corrected in this work.

In the integrated HPEM-DTM model, dust particles are introduced into the reactor after plasma properties (e.g., densities of charged and neutral species) computed by the HPEM have reached a steady state. At that time, after each iteration through the modules of the HPEM, electric fields, neutral and charged particle fluxes and densities, and temperature gradients are exported to the DTM module. These quantities are then used to compute forces on the dust particles and integrate their trajectories. During execution of the DTM (typically for a few to tens of milliseconds which is large compared to the RF period of 100 nanoseconds) the plasma properties obtained from the HPEM are held

constant. At the end of a call to the DTM, dust particle densities and their charge states are returned to the HPEM. The locations of the dust particles are binned on the same numerical mesh as that used in the HPEM, and the densities are distributed on the mesh using finite-sized particle techniques. The dust densities and their charges are then used in the solution of Poisson's equation, and in computing electron and ion transport. Dust densities and charges are held constant during the following iteration through the HPEM. The time spent in the DTM, and the time spent in the HPEM between calls to the DTM, were empirically chosen to be small enough so that holding properties constant in this manner is an acceptable approximation.

Dust particles interact with other plasma species in the HPEM through their charge density which, when included in solution of Poisson's equation, perturbs the electric potential. They also interact by providing surfaces internal to the plasma upon which heterogeneous chemistry can occur, including recombination of charged particles. Particles are also sources of momentum loss for electrons and ions through collisions. The electron-dust collection cross-section included in the EETM for electron energy ε is[10]

$$\sigma_{col}(\varepsilon) = \pi a^2 \left[1 - \frac{e\Phi}{\varepsilon}\right] \tag{3.12}$$

for electron energies greater than $|e\Phi|$. The electron-dust momentum transfer cross-section was evaluated from standard coulomb scattering theory:[10]

$$\sigma_m(\varepsilon) = 4\pi\,\varepsilon_o^2 \;\ln\left[1+\left(\frac{\lambda_L}{b_o}\right)^2\right]^{1/2} \tag{3.13}$$

where b_o is the scattering parameter for 90° collisions. The positive ion flux to the particles was forced to be the same as the cycle-average loss of electrons to the particles.

3.7 Characterization of Coulomb Solids

To quantify the character of dust particle clouds in our plasmas, we utilized two metrics; the Coulomb coupling parameter Γ and the pair correlation function (PCF), g(r). To account for the screened charge on the dust particles due to ions, the Coulomb coupling parameter for a collection of N particles is

$$\Gamma = \frac{1}{N}\sum_{i=1}^{N}\Gamma_i\,, \quad \Gamma_i = \frac{\dfrac{Q_i}{4\pi\varepsilon_o}\;\displaystyle\sum_j \frac{Q_j}{R_{ij}}\;\exp\left(-\frac{R_{ij}-a}{\lambda_L}\right)}{\dfrac{3}{2}\;k\,T_{eff}} \tag{3.14}$$

where T_{eff} is the effective temperature of the particle and R_{ij} is the separation between particles. The effective temperature encompasses both thermal and directed energy, $\frac{3}{2}kT_{eff} = \frac{3}{2}kT + \frac{1}{2}mv^2$. Neglecting fluid drag effects, particles can convert a large fraction of their directed energy into randomized thermal energy due to Coulomb collisions with other particles. Large values of Γ (> tens to hundreds) denote a system, which is dominated by interparticle forces, and so can be classified as a Coulomb fluid (Γ≈ ones to tens) or a Coulomb solid (Γ≈ hundreds).

To examine the phases of the structures that form (solid versus liquid), the PCF is used. The function *g(r)* is the probability of finding two particles separated by a distance

r, as compared to that for an unstructured random distribution of particles. The PCF is calculated using the method described by Quinn et al.[11] A particle is chosen as the center point or test particle. The remaining particles in a specified region are then binned according to their distance from the test particle. These particle counts are then divided by the annular area defined by their distance from the test particle, and are normalized by the resulting average particle density. This procedure is repeated using all the particles in the region as test particles and the results averaged. Successive peaks in *g(r)* at small *r* correspond, respectively, to first, second, and increasing nearest neighbors. The characteristics of the Coulomb crystals in RF discharges are discussed in the following chapter.

3.8 References

[1] H. H. Hwang and M. J. Kushner, J. Appl. Phys. **82**, 2106 (1997).

[2] J. E. Daugherty, R. K. Porteous, M. D. Kilgore, and D. B. Graves, J. Appl. Phys. **72**, 3934 (1992).

[3] M. D. Kilgore, J. E. Daugherty, R. K. Porteous, and D. B. Graves, J. Appl. Phys. **73**, 7195 (1993).

[4] S. A. Khrapak, A. V. Ivlev, G. E. Morfill, and H. M. Thomas, Phys. Rev. E **66**, 46414 (2002).

[5] S. J. Choi and M. J. Kushner, Trans. Plasma Science **22**, 138 (1994).

[6] L. Talbot, R. K. Cheng, R. W. Schefer, and D. R. Willis, J. Fluid Mech. **101**, 737 (1980).

[7] S. K. Friedlander, *Smoke, Dust and Haze* (John Wiley and Sons, New York, 1977).

[8] W. Z. Collison and M. J. Kushner, Appl. Phys. Lett. **68**, 903 (1996).

[9] R. L. Kinder and M. J. Kushner, J. Vac. Sci. Tech. A **19**, 76 (2001).

[10] M. Mitchner and C. H. Kruger, *Partially Ionized Gases* (John Wiley and Sons, New York, 1973).

[11] R. A. Quinn, C. Cui, J. Goree, J. B. Pieper, H. Thomas, and G. E. Morfill, Phys. Rev. E **53**, R2049 (1996).

4. CHARACTERISTICS OF COULOMB CRYSTALS IN RF DISCHARGES

The integrated dust transport module has been used to investigate particle transport and Coulomb crystals in plasma processing reactors. The effect of varying the bias voltage of a capacitively coupled discharge, gas chemistries, particle diameter, and the number of particles on the propensity for crystal formation has been investigated. The model has been validated by comparisons with experimental results.

4.1 Plasma Operating Conditions

The model reactor is a modified Gaseous Electronics Conference (GEC) reference cell schematically shown in Fig. 4.1. The lower electrode is powered at 10 MHz. An annular plate replaced the upper electrode so that, experimentally, particles can be observed from the top of the reactor.[1] A metal washer placed on the lower electrode acts as a focus ring to warp the electric potential into a well to confine the dust particles. The plasma was sustained in argon at 95 mTorr with a flow rate of 300 sccm, which is exhausted through the pump port surrounding the lower electrode. The substrate bias was varied from 125 V to 250 V. (Substrate bias refers to the amplitude of the RF voltage.) Dust particles of mass density 2.33 g cm^{-3} akin to that of amorphous silicon were initially randomly distributed between the electrodes. Their trajectories were integrated for approximately 8 s until they settled into a quasi-stable geometric configuration.

The electron density, electron temperature and the time-averaged plasma potential for a substrate bias of 150 V are shown in Fig. 4.2. The peak Ar^+ density is 1.2×10^{10} cm^{-3} and peak plasma potential is 95 V, including a –7 V dc bias on the substrate. The plasma penetrates through the annular grounded electrode into the upper chamber. The

plasma potential is largely flat in the body of the plasma. Sheaths surround the annulus, and there are large ambipolar electric fields in the periphery of the reactor. The ion density and plasma potential are conformal to the focus ring forming a potential well in which the particles are trapped. Trapped particles are usually confined to this region. Particles not seeded in locations that can access the potential well formed by the focus ring are, for these conditions, eventually expelled from the bulk plasma.

4.2 Influence of RF Power on Crystal Morphology

Typical morphologies of Coulomb crystal lattices, as observed from the top of the reactor through the annular electrode, are shown in Fig. 4.3. Configurations are shown for low (150 V) and high (250 V) substrate biases. At the lower bias, a single disk-shaped lattice of dust particles, 1 layer thick, is obtained which is confined to the center of the potential well. Examination of the PCF and Coulomb coupling factor (discussed below) confirm this structure is a Coulomb solid. In the center of the lattice where the confining forces, largely electrostatic and gravitational compressive forces from particles at larger radii, are largest, the lattice has regular hexagonal structure. In the periphery of the lattice where confining forces are smaller, the structure is less regular. The need to match the hexagonal shape of the plasma crystal to a round confining potential causes some defects to appear. As the bias is increased (>200 V), a void forms in the center of the crystal, resulting in an annular lattice. Voids were created irrespective of the number of initial particles seeded in the system (up to a few hundred), indicating that the formation of the voids is not necessarily a consequence of interparticle forces but rather a consequence of a change in the plasma forces. For example, the radial ion-momentum flux at the level of the particles increased from 2.6×10^{-8} g/cm^{2}s for a 150 V bias to 6.6 ×

10^{-8} g/cm^{2}s for a 250 V bias. We speculate that larger radial ion-drag forces at higher biases are responsible for the formation of a void as noted by Samsonov and Goree.[2] A larger fraction of the initially seeded particles is expelled from the plasma at higher biases as well.

Similar results have been observed experimentally using the apparatus and techniques described in Hebner et al.[1] For this work, the lower electrode with a parabolic shape is replaced by a flat electrode and confinement ring similar to the configuration shown in Fig. 4.1. For example, particle lattices are shown in Fig. 4.4 for similar discharge conditions (Ar, 90 mTorr, 20 MHz, 8.34 μm particles). At low power (1.8 W), the particles form a single layer, disk-shaped lattice with a hexagonal structure. Upon increasing the RF power (34 W), a void is created in the lattice. The asymmetry in the lattice at higher powers occurs because the surfaces of the electrode and focus rings may not be perfectly leveled and the particles tend to slide down hill or there is azimuthal asymmetry in the plasma.

4.3 Effect of Particle Size on Crystal Morphology

The influence of particle size on the morphology of Coulomb crystals was investigated by varying the particle radius from 0.1 μm to 10 μm while keeping the number of particles in the lattice constant at 150. For typical conditions (Ar, 95 mTorr, 150 V), two classes of particle lattices are shown in Fig. 4.5. We observe two distinct and well-separated structures for smaller particles, such as the 0.1 μm particles shown in Fig. 4.5(a). The upper structure is disk-shaped and well above the upper electrode. Particles are trapped at this location due to a balance between the downward pointing electrostatic and upward directed ion-drag forces, as gravitational forces are not

important for these small particles. Some particles get seeded in the potential well near the bottom electrode and form a ring-shaped structure at a lower location, though at height well above the focus ring. As we increase the size of the particles to 10 μm (Fig. 4.5(b)), the upper lattice disperses, as the weak ion drag forces in the periphery of the plasma cannot balance gravitational forces. The 10 μm particles arrange themselves in a single disk shaped lattice at a lower height than the smaller particles, a consequence of both their larger mass and larger ion drag forces. There are isolated instances in the edge-on view of Fig. 4.5(b) where there appear to be two layers to the lattice. The lattice is actually only a single layer. These displaced particles are isolated particles undergoing vertical oscillatory motion, a phenomenon observed by Tomme et al.[3]

4.4 Dust Particle Oscillations

As dust particles settle into the potential well forming a Coulomb solid, the resulting lattice often oscillates about an equilibrium position. These radial, horizontal oscillations are the result, in part, of the mutual repulsion of the particles in the presence of a restoring force, in this case both gravity and electrostatic plasma forces. Here a radially outward ion drag force also augments the repulsive force. For typical conditions (Ar, 95 mTorr, 10 W, 4 μm particles), we observe an oscillation frequency of 5 Hz. One complete cycle of such oscillations is shown in Fig. 4.6. This collective motion is similar to experimentally observed cooperative oscillation also known as a "breathing mode." For example, Melzer et al.[4] have observed similar behavior using pulse modulation of the RF electrode voltage to initiate the oscillation. The oscillations observed by Melzer et al. damp more quickly then those predicted from our model. Our longer-lived oscillations

appear to be a result of feedback from the plasma electrostatics, which reinforces these largely radial modes.

4.5 Effect of Plasma Density on Crystal Morphology

The consequences of plasma density on interparticle spacing and Coulomb coupling factor were also investigated by artificially increasing ion and electron densities while keeping other conditions constant. Interparticle spacing was determined by the first peak in *g(r)*. The results of this parameterization are summarized in Fig. 4.7 where Coulomb coupling factor and interparticle spacing are shown as a function of electron density. Recall that above a critical plasma density where the particles do not significantly deplete negative charge in the plasma, the charge on particles is only a function of the electron and ion temperatures. The effect of increasing the plasma density is primarily to change the shielding length. As the plasma density increases, λ_L decreases, thereby reducing the interparticle separation for which a given force is experienced. The end result is a decrease in interparticle spacing. More aggressive shielding produces less electrostatic interaction and a decrease in the Coulomb coupling factor. The exception is at low plasma densities where the interparticle spacing increases because of an increase in the particle temperature. This increase in particle temperature is responsible for the large initial drop in the Coulomb coupling factor, which then more slowly decreases commensurate with the decrease in shielding length.

4.6 Interparticle Spacing in the Coulomb Crystal

The consequence of the number of particles on interparticle spacing was also investigated. The first, nearest neighbor peak of *g(r)* was used to determine the average particle separation. The function *g(r)* for base case conditions is shown in Fig. 4.8 for

lattices having 7 and 200 particles. Top views of these lattices, and for 500 particles, are shown in Fig. 4.9. Computed interparticle separations for 3.8 μm particles as a function the number of particles in the lattice are shown in Fig. 4.10(a), and result for similar experimental conditions are shown Fig. 4.10(b). In general, increasing the number of particles in a lattice produces a monotonic decrease in particles spacing. Increasing the number of particles in the lattice generally decreases the interparticle spacing, as more particles accessing a finite-sized potential well leads to radial compression of the plasma crystal. The function *g(r)* for the smaller crystal has well defined peaks due to the near perfect hexagonal arrangement of the particles. The function *g(r)* for the larger crystal has less well defined peaks due to the propensity for dislocations and the fact that the particle spacing is a function of radius in the crystal. For example, nearest neighbor spacing as a function of radial position for a plasma crystal containing 200 particles is shown in Fig. 4.10(c). The nearest neighbor spacing is smallest in the center of the crystal where the compressive forces of particles at larger radii is the largest, and these forces add to the radial plasma forces which provide the overall confinement for the lattice. As one moves to larger radii, the compressive forces due to outlying particles lessens, leaving only the plasma confining forces, producing a larger interparticle separation. Similar results have been reported by Hebner et al.[1,5,6] The Coulomb coupling factor increases with an increase in the number of particles because due to the decrease in interparticle spacing and a decrease in the particle temperature, as shown in Fig. 4.11.

There is no clear correlation between the substrate bias and the interparticle spacing as several competing effects come into play. An increase in bias leads to higher

plasma densities and so a reduced shielding length should produce smaller interparticle spacing. However, particle temperatures tend to be larger at higher biases, and that effect should produce larger interparticle spacings. The interparticle spacing decreased with an increase in the number of particles for all biases we examined; however, for a fixed number of particles the trend was not monotonic with increasing bias.

4.7 Coulomb Crystals in Electronegative Plasmas

The morphology of Coulomb crystals in electronegative plasmas has been the focus of recent investigations.[7] The negative ion density in an electronegative plasma can often greatly exceed the electron density. As a consequence, the ion drag force acting on the dust particles and the charge on particles can be different, leading to qualitatively different crystal morphologies than those found in electropositive plasmas. To investigate the effect of negative ions on crystal morphologies, O_2 and Cl_2 were added to Ar in various proportions. For example, crystal morphologies for pure Ar and Ar/Cl_2 = 90/10 are compared in Fig. 4.12. For pure Ar, the particles settle in a ring-shaped configuration. On increasing the Cl_2 fraction to 0.1, the void closes, and the particles settle into a single, small disk-shaped structure. More particles are also lost from the plasma.

The cause for this behavior is ultimately rooted in the electron density and ion momentum flux vectors, as shown in Fig. 4.13. The peak electron density in the reactor decreased from 3×10^{10} cm^{-3} for Ar to 6×10^{8} cm^{-3} for Ar/Cl_2 = 90/10 while the ion density remains roughly constant. The resulting increase in the sheath thickness in the electronegative plasma decreased the peak electrostatic fields in the sheath from 280 V/cm for pure Ar to 145 V/cm for Ar/Cl_2 = 90/10. The charge on the dust particles is

smaller in the electronegative mixture due to the increase in the positive ion flux relative to the electron flux. The reduction in charge combined with the smaller electric fields in the sheath leads to reduced electrostatic shielding and larger propensity for particles not to be trapped. The shape of the crystals is dominantly a function of a change in the direction of the ion momentum flux. The mass averaged ion momentum flux exerts an outward ion-drag on the particles in pure Ar, which leads to the formation of a void (see Fig. 4.13(a)), whereas in Ar/Cl_2 plasmas, the net ion-momentum flux pushes particles to the center of the reactor and causes the void to close (see Fig. 4.13(b)).

A similar result is observed in Ar/O_2 for oxygen fractions of 0.0 to 0.6. The reduction in electron density on increasing the oxygen fraction is less than for Ar/Cl_2 plasmas as oxygen is a less electronegative gas than chlorine. For example, the peak electron density varied from 3.5×10^9 cm^{-3} for $Ar/O_2 = 80/20$ to 1×10^9 cm^{-3} for $Ar/O_2 = 40/60$. The resulting plasma crystal morphology for these cases is shown in Fig. 4.14. Although in Ar/Cl_2 the ring structure collapsed to a disk with only 10% admixture of Cl_2, the ring structure in Ar/O_2 is maintained to mole fractions exceeding 50%. With sufficient Ar/O_2 addition, the ion momentum flux eventually transitions from being radially outward to radially inward, and the crystal morphology transitions from a ring to a disk. These results are in agreement with experimentally observed trends.[7]

4.8 Conclusions

A self-consistent 3-D model has been developed to investigate particle transport and Coulomb crystal formation in plasma processing reactors. The propensity for crystal formation as a function of various process parameters such as substrate bias, gas chemistries and particle size and number were discussed. In particular, we found that the

Coulomb crystal typically contained a void at high substrates due to the larger ion drag forces. These ring-like structures collapsed to a disk upon addition of electronegative gases like Cl_2 and O_2, commensurate with a shift in the net ion momentum flux vectors to having a radially inward component. The interparticle spacing decreases on increasing the number of particles in the lattice due to larger compressive forces from particles at larger radii. Larger particles settle closer to the sheath as higher electrostatic fields are required to offset the effects of gravity. The dust particles exhibit cooperative oscillation as they settle in the potential well.

4.9 Figures

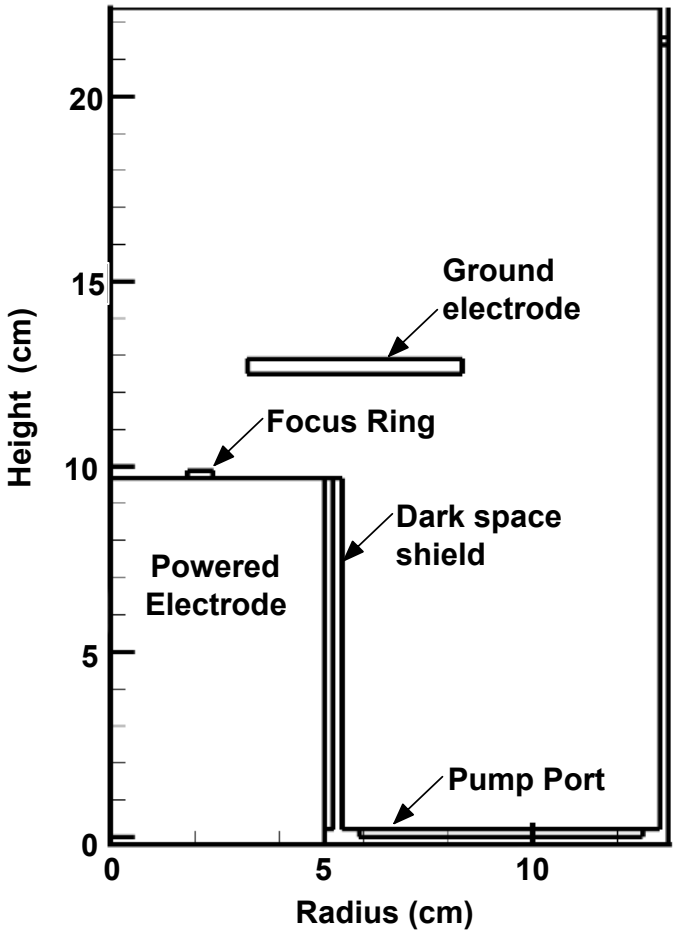

Fig. 4.1. Schematic of the modified GEC reference cell used in the simulations.

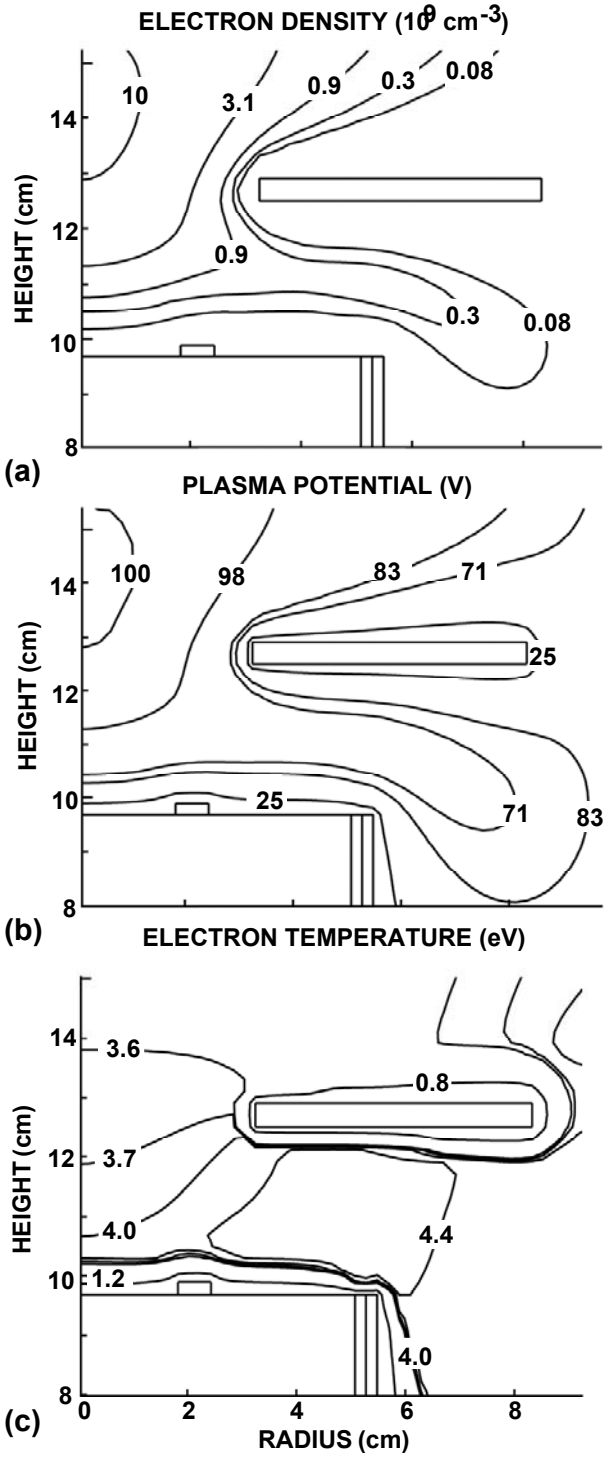

Fig. 4.2. Plasma properties in an Ar discharge (95 mTorr, 300 sccm) for a substrate bias of 150 V: (a) electron density, (b) plasma potential, and (c) electron temperature.

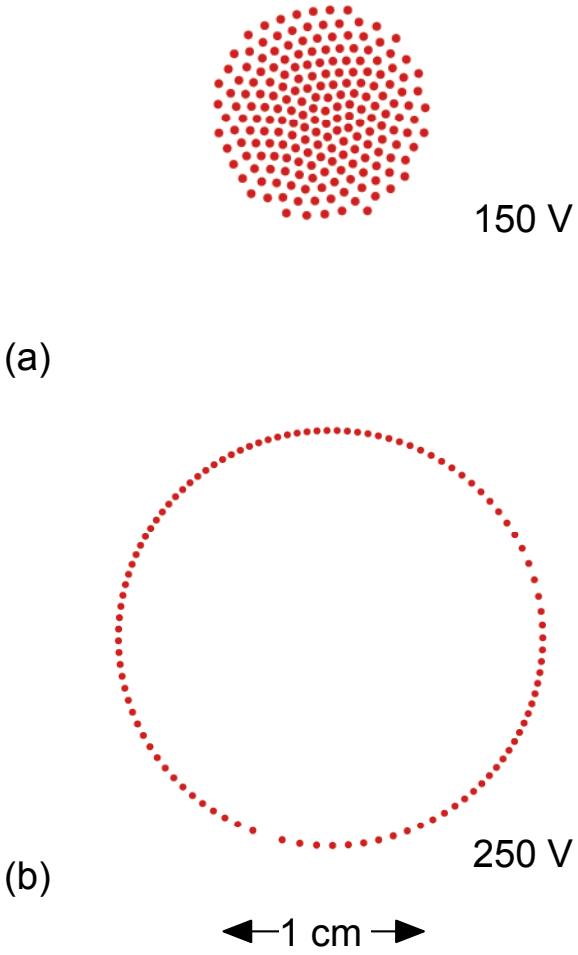

Fig. 4.3. Top view of particle positions (4.9 μm) in an Ar discharge (95 mTorr, 300 sccm): (a) Particles arrange in a central disk for a bias of 150 V. (b) A void is formed at higher biases, shown here for 250 V.

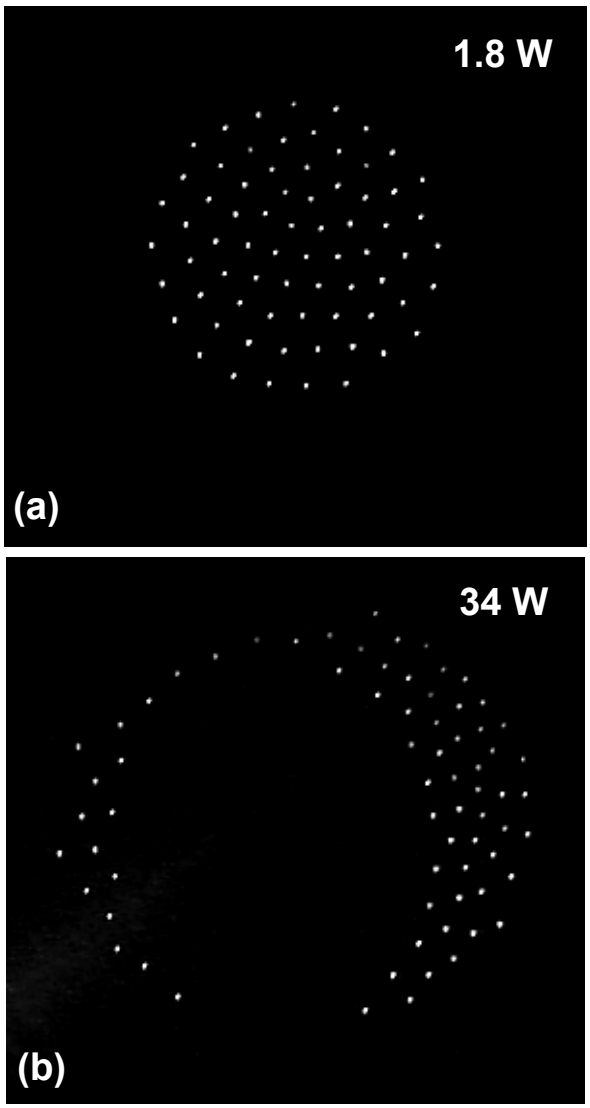

Fig. 4.4. Experimental results for the evolution of void in a Coulomb crystal for an Ar, 90 mTorr, 20 MHz plasma: (a) 1.8 W, and (b) 34 W.

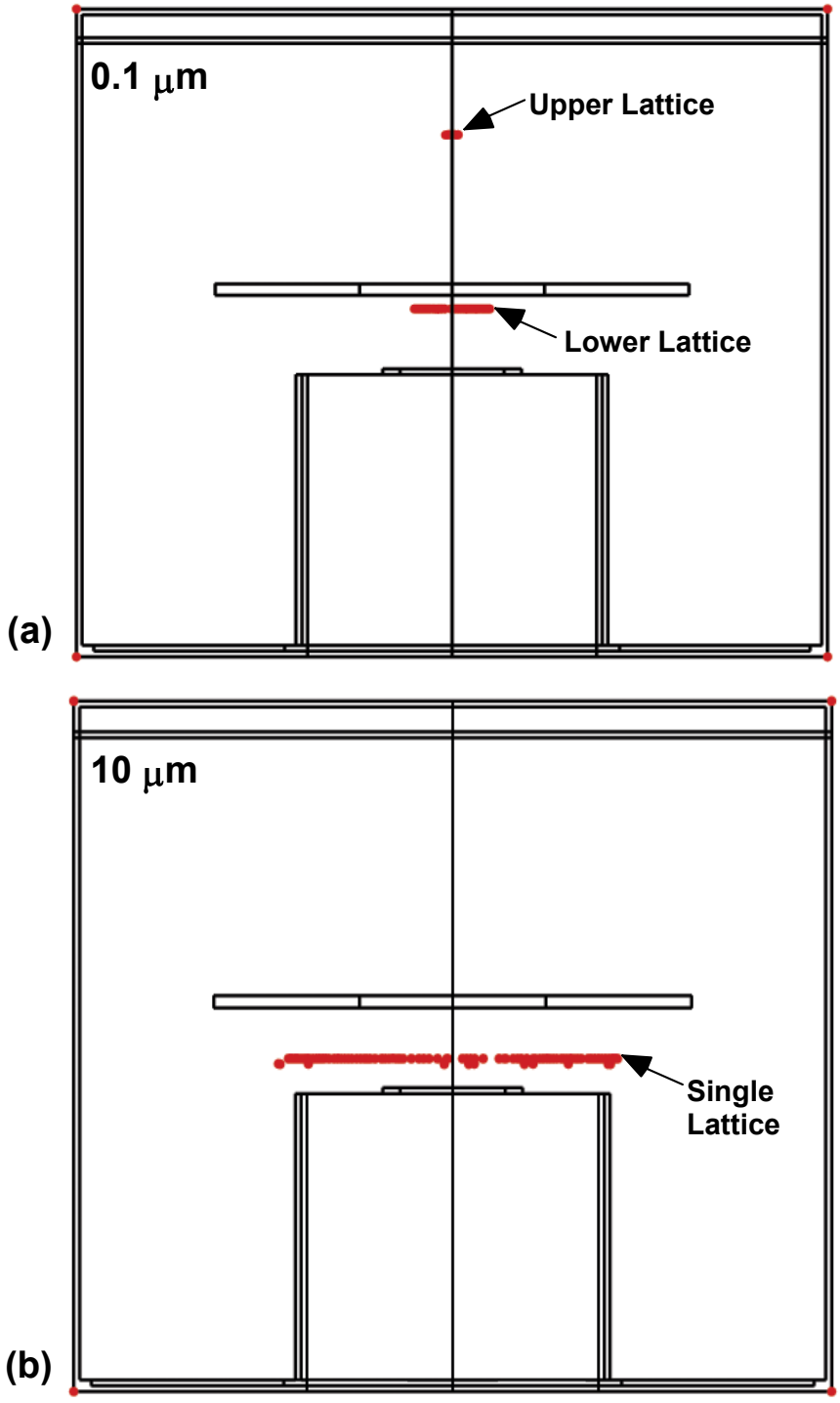

Fig. 4.5. Effect of particle size on trapping positions in an Ar discharge (95 mTorr, 300 sccm, 150 V): (a) 0.1 μm particles arrange in two lattices, and (b) 10 μm particles arrange in a single lattice close to the powered electrode.

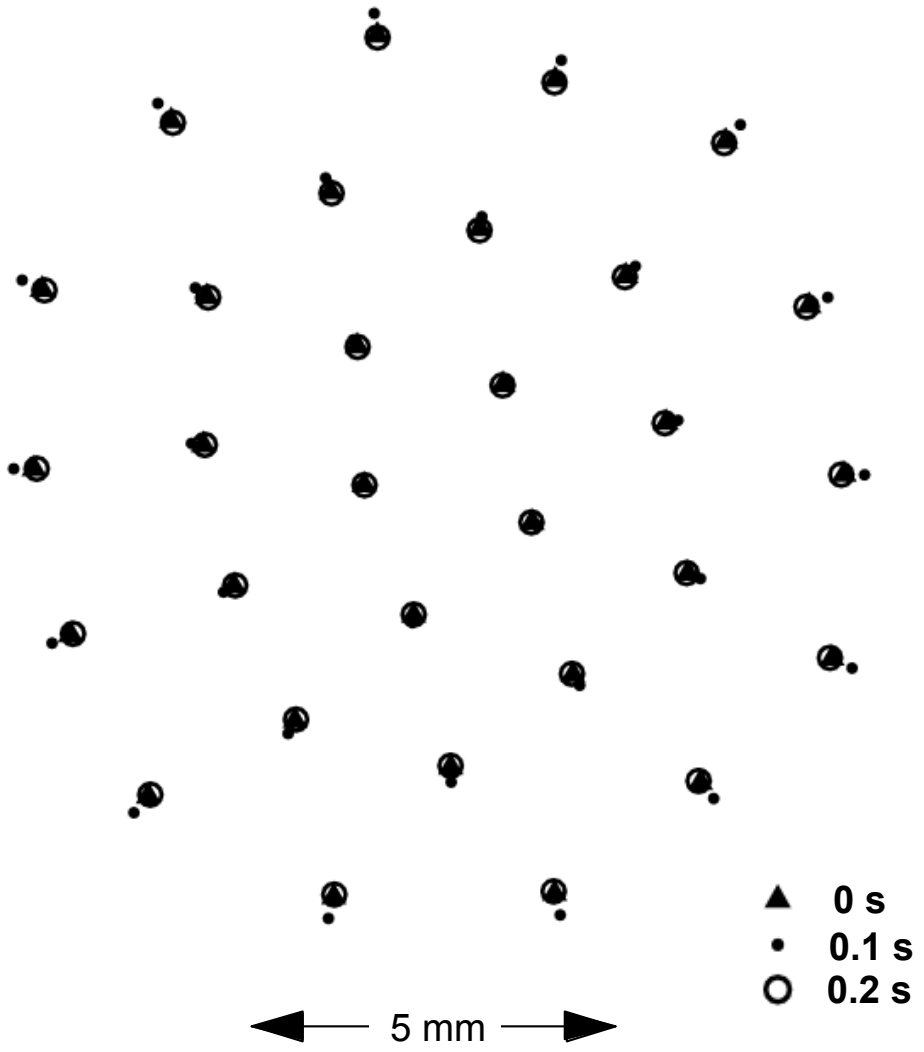

Fig. 4.6. Horizontal oscillations (5 Hz) of particles in an Ar discharge (95 mTorr, 10 W, 4 μm particles). Particle positions are shown at different times during one complete cycle. Cooperative oscillation of particles such as this is often referred to as a "breathing mode."

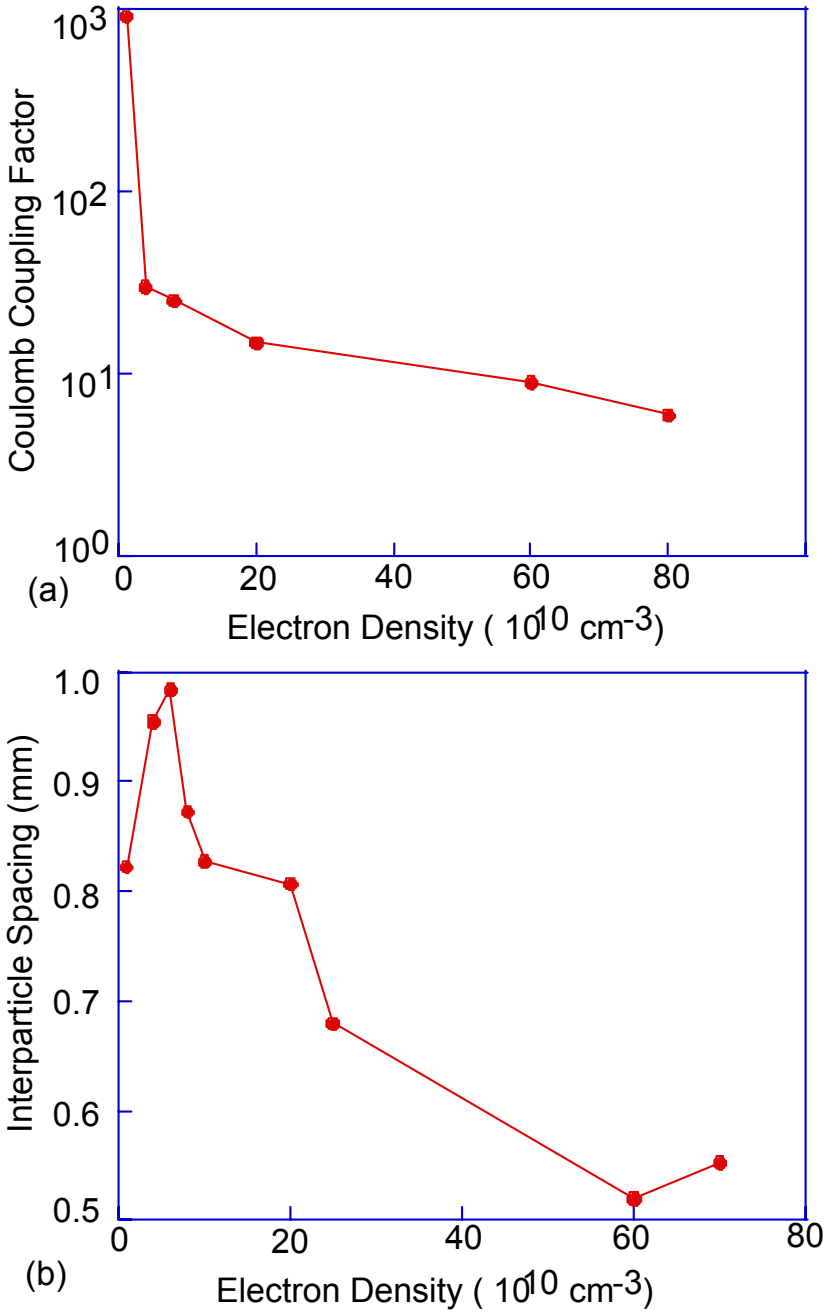

Fig. 4.7. Effect of plasma density on the (a) Coulomb coupling factor and (b) interparticle spacing. Ion and electron densities were varied keeping other conditions constant in an Ar discharge (95 mTorr, 300 sccm, 150 V).

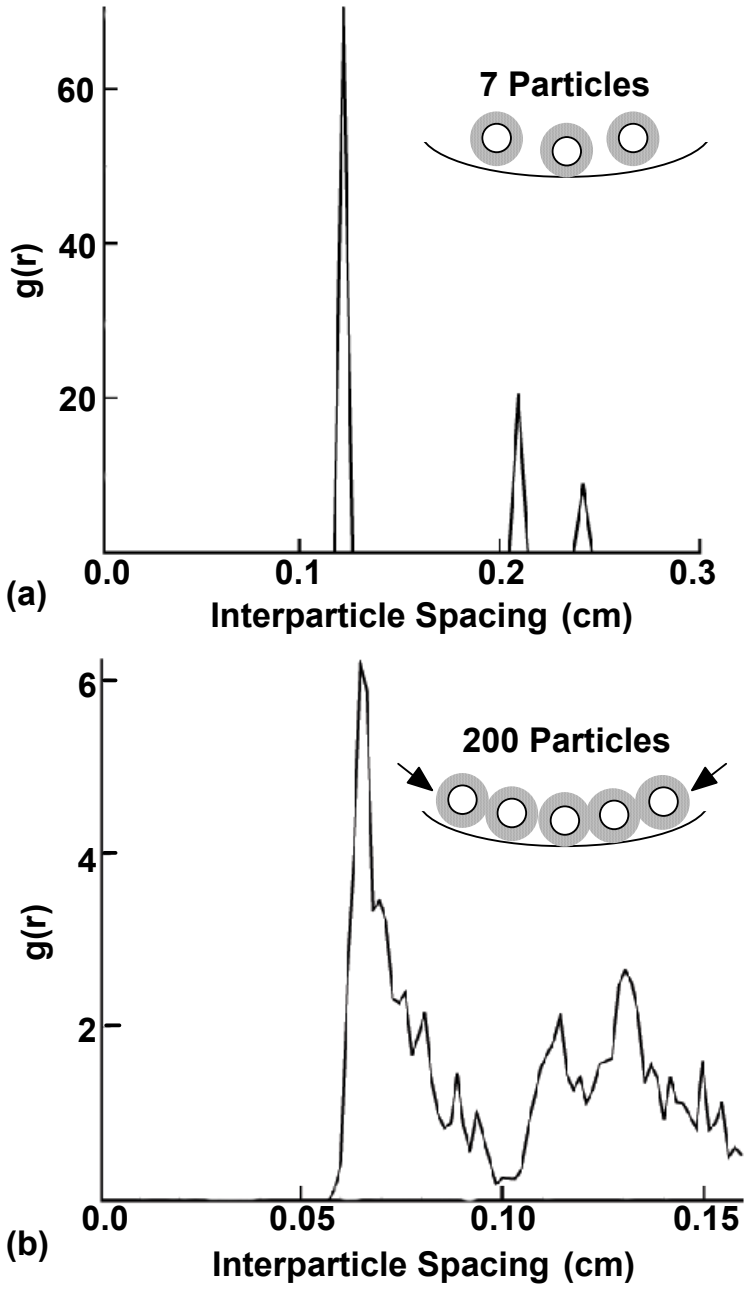

Fig. 4.8. Effect of particle number on PCF in an Ar discharge (95 mTorr, 300 sccm, 150 V, 3.8 μm particles): (a) 7 particles, and (b) 200 particles. The first nearest neighbor peak is shifts to lower values on increasing the number of particles.

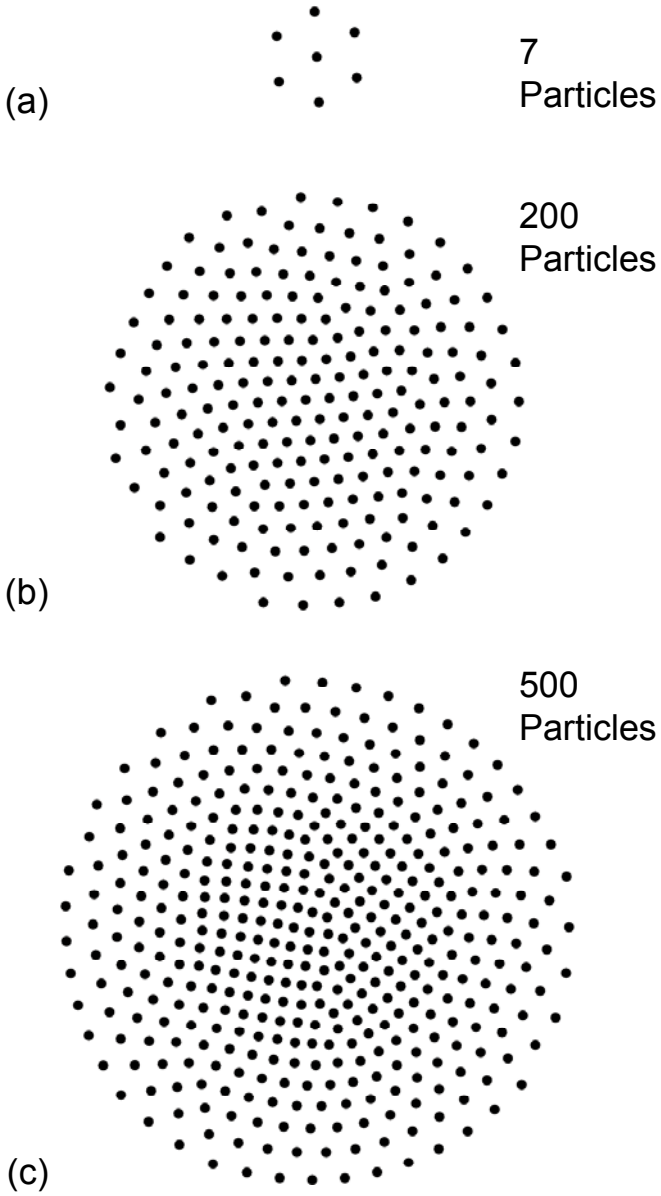

Fig. 4.9. Top views of the particle crystal for (a) 7 particles, (b) 200 particles, and (c) 500 particles. Interparticle spacing is smaller in the center of the larger crystals due to compressive forces from particles at larger radii.

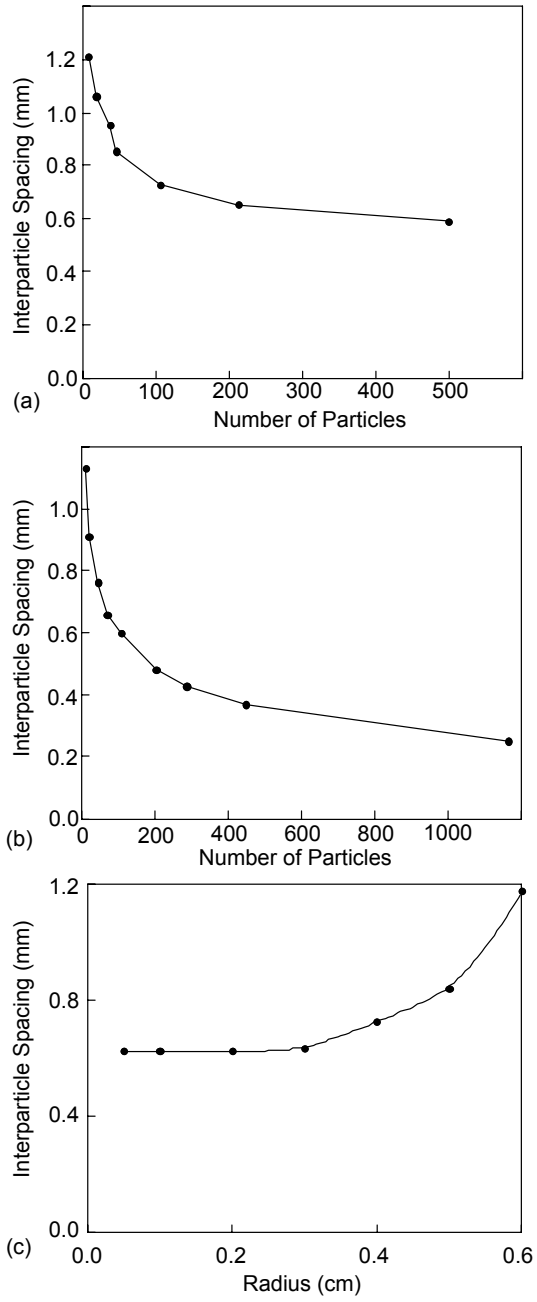

Fig. 4.10. Interparticle spacing for 3.8 μm particles (Ar, 95 mTorr, 300 sccm): (a) computed distances as a function of the number of particles in the lattice, (b) experimentally observed interparticle spacing in an Ar, 110 mTorr, and 1.8 W plasma,[6] and (c) computed nearest neighbor separation as a function of radial position for Coulomb crystal containing 200 particles.

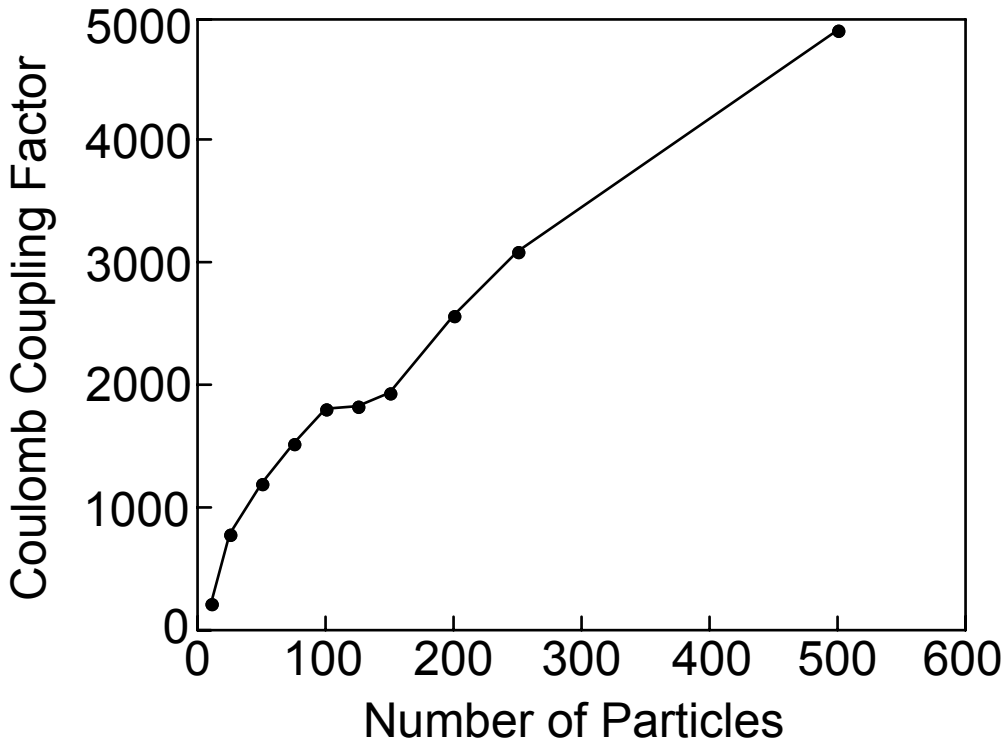

Fig. 4.11. Coulomb coupling factor as a function of the number of particles in an Ar discharge (95 mTorr, 300 sccm, 150 V).

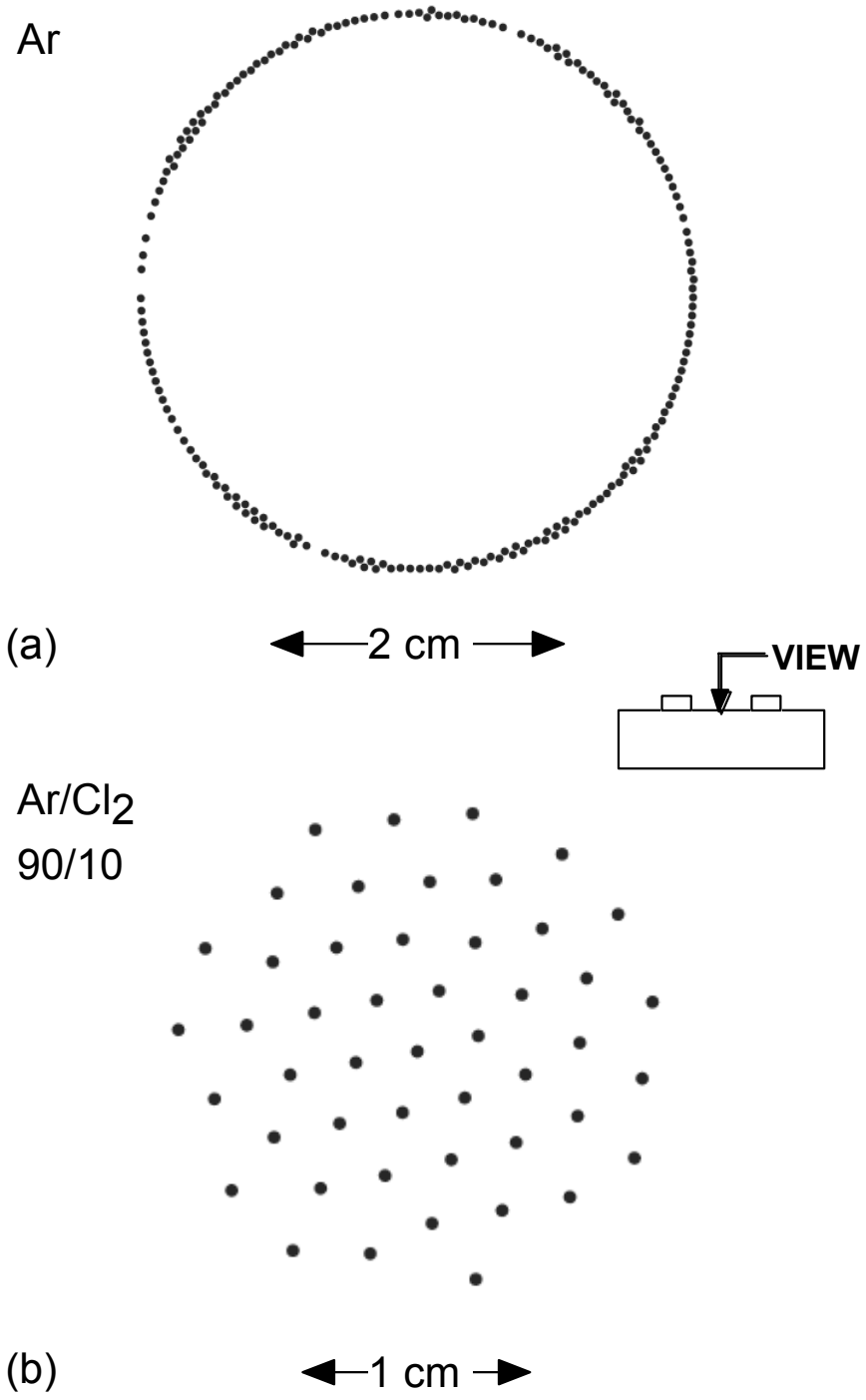

Fig. 4.12. Plasma crystal morphologies in an Ar/Cl_2 discharge (14 sccm, 0.14 Torr, 40W): (a) pure Ar, and (b) Ar/Cl_2 = 90/10. Addition of Cl_2 causes the plasma crystal void to close.

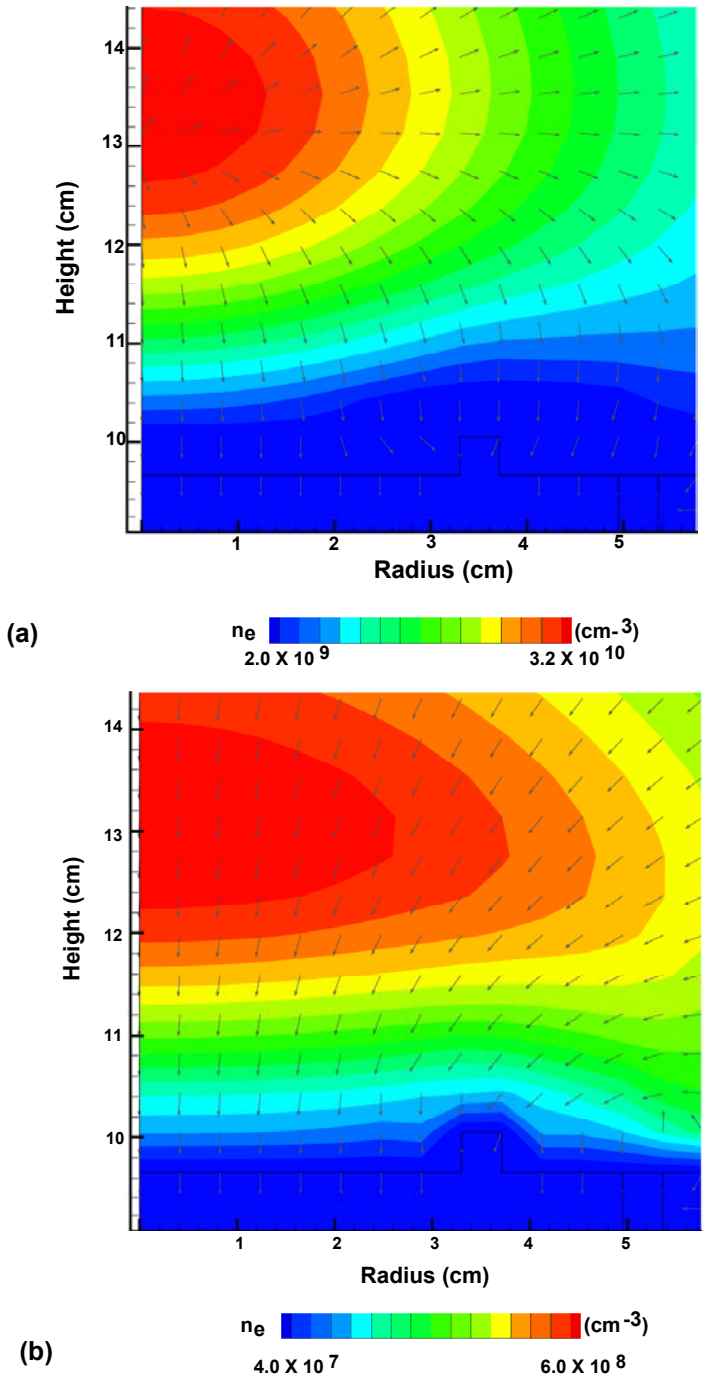

Fig. 4.13. Electron density and ion-momentum-flux vectors in RF discharge (14 sccm, 0.14 Torr, 40W): (a) pure Ar, and (b) Ar/Cl_2 = 90/10. The reorientation of the ion momentum flux vectors upon addition of electronegative gas causes the void to close.

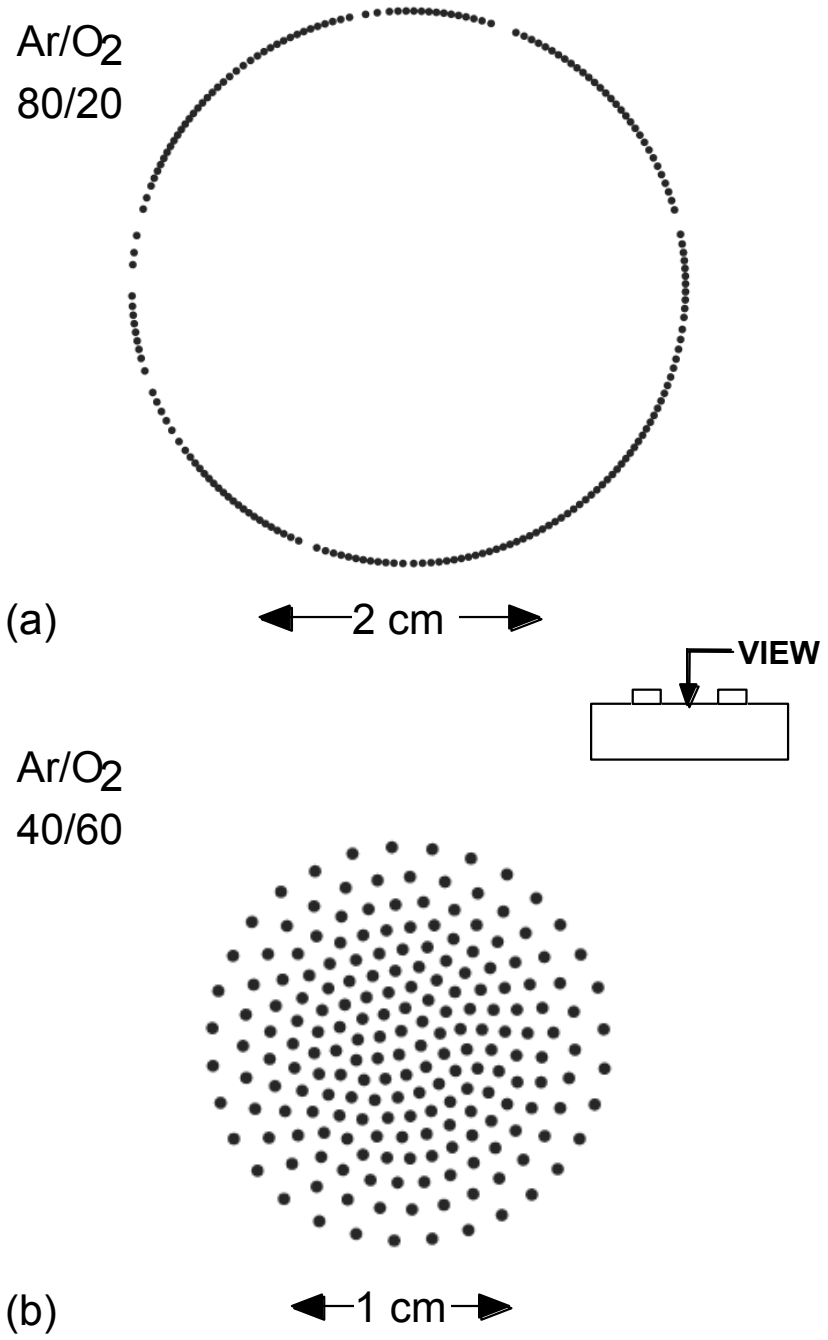

Fig. 4.14. Plasma crystal morphologies in an Ar/O_2 discharge (14 sccm, 0.14 Torr, 40W). (a) Ar/O_2 = 80/20 wherein a void is formed in the plasma crystal because of the larger ion-drag forces. (b) Ar/O_2 = 40/60 wherein the void in the plasma crystal closes.

4.10 References

[1] G. A. Hebner, M. E. Riley, D. S. Johnson, P. Ho and R. J. Buss, Phys. Rev. Lett. **87**, 235001 (2001).

[2] D. Samsonov and J. Goree, Phys. Rev. E **59**, 1047 (1999).

[3] E. B. Tomme, B. M. Annaratone, and J. E. Allen, Plasma Sources Sci. Technol. **9,** 87 (2000).

[4] A. Melzer, M. Klindworth, and A. Piel, Phys. Rev. Lett. **87**, 115002 (2001).

[5] G. A. Hebner, M. E. Riley, D. S. Johnson, P. Ho, and R. J. Buss, IEEE Trans. Plasma Sci. **30 (1)**, 94 (2002).

[6] G. A. Hebner, M. E. Riley, and K. E. Greenberg, Phys. Rev. E. (submitted for publication).

[7] R. P. Dahiya, G. Paeva, W. W. Stoffels, E. Stoffels, G. M. W. Kroesen, K. Avinash, and A. Bhattacharjee, Phys. Rev. Lett. **89**, 125001 (2002).

5. EFFECT OF ION STREAMING ON CRYSTAL MORPHOLOGY

5.1 Introduction

Dust particles in low temperature, low pressure plasmas form Coulomb crystals and display collective behavior under select conditions. Ion drag forces, important sources of acceleration for these particles, result from long-range Coulomb interactions. The trajectories of ions are perturbed as they pass by the negatively charged dust particles and, in some cases, converge beyond the particle. This process, called *ion streaming*, results in positive potential in the wake of the particle that can be large enough to significantly affect interparticle dynamics.

When the particle count is large and the potential well deep, more complex 3-D assemblies of the dust particles have been observed with a range of order from face- and body-centered cubic lattices to more amorphous arrangements.[1,2] Weakly interacting vertical strings of grains have also been observed.[3,4] These phenomena are not easily explained on the basis of the repulsive Debye potential and may be, in part, attributed to ion streaming. Ion streaming results from positive ions flowing past and focusing beyond negatively charged particles, generating wake fields of positive space charge. The typical geometry is for particles to be trapped in horizontal layers near the edge of the sheath. Positive ions, accelerated by the presheath and the sheath, perpendicularly intersect these layers as the ions proceed towards the boundary of the plasma. The positive space charge in the wake field below particles trapped at the sheath edge can be sufficiently large that particles at lower heights are attracted to that location, thereby producing vertical

correlations between particles. In this regard, Samsonov et al.[5] recently observed a nonreciprocal attractive interaction between two particles of different masses. The interaction is a sum of two forces: the repulsive electrostatic force, which prevails at short distances and the attractive ion streaming force, which prevails at longer distances. Hebner et al.[6] have measured the attractive and repulsive components of the interaction force. They found that the structure of the ion-wakefield-induced attractive potential was significantly different than a screened-Coulomb repulsive potential and was responsible for the instabilities observed in multilayer assemblies.

Lampe et al.[7] developed an expression for the ion shadowing force by deriving the ion-momentum intercepted by the upstream particle. In this formulation, the ion shadowing force scales linearly with the ion density and is an inverse square force as is the bare Coulomb force. They observed that the range of attractive force shrinks to zero in regimes of relatively low plasma density, high gas pressure, and small particle sizes. Recently, Khrapak et al.[8] investigated the relative magnitudes of the shadowing forces associated with ions and neutrals in the isotropic bulk plasma and the plasma sheath region. They obtained analytical expressions for the resulting interaction potential and noted that neutral shadowing is of minor importance under most conditions of interest.

In this chapter, the effects of ion streaming on the morphology of Coulomb crystal are reported. The ion streaming formulation used for this study is discussed in Section 5.2, followed by results in Section 5.3.

5.2 Ion Streaming Force

In addition to the interparticle Coulomb force and conventional ion drag terms, we also included a shadowing or ion streaming force between particles. Perturbation of

ion trajectories by adjacent particles produces an electric potential in the wake of the upstream particle leading to an attractive force to nearby negative particles. Lampe et al.[7] derived an expression for the shadowing force in an isotropic plasma,

$$F_S = -\frac{3}{8}\frac{a^2}{\lambda_{Di}{}^2}\frac{Z^2e^2}{d^2}, \quad \lambda_{Di} = \left(\frac{4\pi N_I e^2}{T_i}\right)^{-1/2}, \tag{5.1}$$

where Z is the particle charge, T_i is the ion temperature, and d is the interparticle separation.

In an anisotropic plasma, the velocity vectors of ions have a net directionality. For example, ions entering the presheath are accelerated to speeds characteristic of the electron temperature in a direction perpendicular to the electrode. It is, in fact, this anisotropic ion velocity distribution, which produces the angularly dependent wakefield charge distribution that produces vertical correlations between particles. The derivation of a general expression for the anisotropic ion streaming force was beyond the scope of this work. To capture the properties of such an anisotropic force, we made the following adaptation and approximation to Lampe's expressions.

We assume that the total ion streaming force $\vec{F}_{ST}$ is the sum of the force due to isotropic thermal fluxes of ions $\vec{F}_S$ and a force due to a directed anisotropic ion flux $\vec{F}_D$. The direction of $\vec{F}_S$ is parallel to the interparticle chord, whereas the direction of $\vec{F}_D$ is the chord between the particle and the center of the wakefield charge distribution. The magnitude of $\vec{F}_D$ should scale linearly with the magnitude of the anisotropically

distributed positive charge that the directed ion flux creates relative to the isotropic ion flux.

We assumed that the isotropic ion streaming force could be represented by a ring of positive space charge density n^+ around the dust particle. The magnitude of the positive space charge is,

$$n^+ = \varepsilon_0 \frac{\partial^2 \Phi}{\partial r^2}, \quad \text{where} \quad \frac{\partial \Phi}{\partial r} = \frac{F_S}{Q} \tag{5.2}$$

We then approximate that the positive space charge density is equivalent to a net charge N^+ residing a distance R from the particle,

$$N^+ = \int_a^{a+\lambda_D} n^+ 4\pi r^2 \, dr \tag{5.3}$$

$$R = \frac{\int_a^{a+\lambda_D} r \, n^+ 4\pi r^2 dr}{\int_a^{a+\lambda_D} n^+ 4\pi r^2 dr} = \frac{\lambda_D}{\ln\left(\frac{a+\lambda_D}{\lambda_D}\right)} \tag{5.4}$$

The magnitude of the space charge due to the anisotropic directed ion flux is then

$$N_D{}^+ = \frac{\Phi_D}{\Phi_R} N^+ \tag{5.5}$$

where Φ_D and Φ_R are the magnitudes of the directed and random thermal ion fluxes. The location of the anisotropic charge resulting from an anisotropic ion streaming past a particle at position $\vec{r}_i$ is

$$\vec{r}_{N^+} = \vec{r}_i + \frac{\vec{\Phi}_D}{\Phi_D} R \tag{5.6}$$

where $\vec{\Phi}_D$ is the anisotropic flux vector. The total ion streaming force on particle j having charge Z_j is then

$$\vec{F}_{ij} = F_S \frac{r_i - r_j}{|r_i - r_j|} + \frac{\vec{r}_{N^+} - \vec{r}_j}{\left|\vec{r}_{N^+} - \vec{r}_j\right|} \frac{{N_D}^+ Z_j}{4\pi\varepsilon_0 \left|\vec{r}_{N^+} - \vec{r}_j\right|^2} \tag{5.7}$$

For computational convenience, interparticle forces are included only if the particles are within a specified distance of each other. There is little qualitative difference in the results for interacting distances greater than $3\lambda_L$. Hence the maximum interaction distance was set to $5\lambda_L$ in order to include sufficient interactions with particles while avoiding unnecessarily large computational times.

5.3. Characteristics of Coulomb Crystals

The model reactor is a modified GEC reference cell schematically shown in Fig. 5.1(a). The lower electrode is powered at 10 MHz. An annular plate replaced the upper electrode so that, experimentally, particles can be observed from the top of the reactor. A metal washer placed on the lower electrode acts as a focus ring to warp the electric potential into a well to confine the dust particles. The plasma was sustained in Ar at 140 mTorr with a flow rate of 15 sccm, which is exhausted through the pump port surrounding the lower electrode. The RF power was varied from 0.1 W to 1 W. Dust particles of mass density 2.33 g cm^{-3} akin to that of amorphous silicon were initially randomly distributed between the electrodes. Their trajectories were integrated until they settled into a quasi-stable geometric configuration. The electron density in the vicinity of the focus ring for an RF power of 1 W is shown in Fig. 5.1(b). The peak Ar^+ density is

10^9 cm^{-3}. The ion density and plasma potential conform to the focus ring forming a potential well in which the particles are trapped.

Typical morphologies of Coulomb crystal lattices composed of 100 particles when excluding the ion streaming force, as observed from the side and top of the reactor, are shown in Fig. 5.2. The particles settle into closely spaced layers with a uniform spacing of approximately 0.06 cm. Due to the finite geometrical size of the potential well, the particles cannot be accommodated in a single layer and so segregate into three layers. The top view of the crystal, Fig. 5.2(b), viewing all layers, displays a hexagonal structure. The structure is, however, not static. Having thermal energy which is "pumped" by the discharge and Debye shielded repulsion, the particles move in and out of the layers. A particle injected into an already filled layer results in the ejection of a particle. Within a given layer, the crystal has a hexagonal structure with voids corresponding to the particle positions in adjacent layers. For example, the individual layer shown in Fig. 5.2(c), the middle layer has vacancies, which mirror locations in the adjacent layers.

The crystals, which result when including the ion streaming force, for otherwise identical conditions, are shown in Fig. 5.3. Particles form several more distinct layers for the same number of particles, as shown by the side view of Fig. 5.3(a). Occasionally and depending on the number of particles and initial positions, vertical strings of particles can be produced. The crystal morphologies, as viewed from the top of the reactor are shown in Fig. 5.3(b) for all layers and in Fig. 5.3(c) for a middle layer. These crystals appear less ordered than in the absence of the streaming force. To quantify the order and the phases of these structures (solid versus liquid), the PCF, *g(r)* was used. The function

g(r) is the probability of finding two particles separated by a distance *r*, as compared to that for an unstructured random distribution of particles. The PCFs with and without the ion streaming force for the conditions of Figs. 5.2 and 5.3 are shown in Fig. 5.4. The periodic structure, with leading major peak of *g(r)* without the streaming force indicates short-range order. The lack of such peaks with the ion streaming force indicates lack of short-range order. The crystal is less ordered when including the ion streaming force. In this regard, Hammerberg et al.[9] have performed molecular dynamics simulations of Coulomb crystal formation in dusty plasmas. They noted that including forces due to the wake potential leads to an amorphous structure that is dominated by vertical strings, rather than true 3-d crystal lattices. Our observations lead to a similar conclusion.

The less ordered crystal obtained when including ion streaming forces could result from there being more vacancies in the larger volume of the crystal. The particles are, on the average, more distant from their neighbors and so less likely to condense into an ordered phase. In this regard, we increased the number of particles to 400 and examined the crystals with and without the ion streaming force. Top views of the plasma crystal at different times, in the absence of the ion streaming force, are shown in Fig. 5.5. It turns out that 400 particles cannot be accommodated in the finite-sized potential well, and as a result some particles (~150) are expelled from the reactor. The top view of the final configuration is shown in Fig. 5.5(c) and the side view is shown in Fig. 5.5(d). The order of the crystal improves on increasing the number of particles, as can be seen in Figure 5.6(a). As we increase the number of particles, the compressive force acting on particles from particles at larger radii increases. This limits motion, thereby producing order within a layer and also forces particles to move to adjacent layers. The PCF in the

axial direction *g(z)* of the crystal shown in Fig. 5.6(b). In the absence of the attractive ion streaming force, the number of layers is small, as particles still prefer the "disk" configuration as opposed to the "string" configuration.

The corresponding morphologies when the ion streaming force is included are shown in Fig. 5.7. On increasing the number of particles, particles settle in more sparsely populated layers than forming fully filled ones, as the vertical force produced by the streaming ions is stronger than the radial compressive force. In a given layer, *g(r)* has an amorphous structure indicating little order as shown in Fig. 5.8, whereas *g(z)* shows well-defined peaks indicating order in the *z* direction. This disparity primarily results from the number of particles being insufficient to fully populate each layer. In the absence of the constraining force, which results from a fully populated layer, particles diffuse within the horizontal plane. This effect is more pronounced in the uppermost layers. Layers lower in the lattice have more order than the upper layers, a phenomenon also noted by Zuzic et al.[10] The weight of the particles in overlying layers compresses the lower layers and decreases the average interparticle spacing. As a result, the Coulomb coupling factor (Γ) increases, as shown in Fig. 5.9.

Ion streaming effects are more significant for larger particle sizes. Larger particles scatter the ions more effectively, a consequence of their larger cross-sections as well as larger charges. For example, side and top views of the plasma crystal for 100 0.1 μm particles is shown in Fig. 5.10 (Ar, 140 mTorr,1 W rf power). 0.1 μm particles are trapped higher in the reactor (2 cm higher than 1 μm particles) due to their smaller masses. At this location, ion streaming is less important than near the sheath edge as the ion flux and speed are both smaller. Similar results have been predicted by Zuzic et al.[10]

Most of the particles are found in the 2 central layers, though some stray particles are trapped in lower layers. Comparing Figs. 5.3 and 5.10 we note that 1 μm particles show a greater propensity to form three-dimensional structures. The crystal is more ordered for 0.1 μm particles. Larger particle sizes (>1 μm) cannot be trapped in the reactor at1 W as the electrostatic shielding is insufficient to offset gravity at lower powers.

Recently Hebner et al.[6] measured the attractive and repulsive components of the interaction force from a trajectory analysis of dust particles collisions in a well-defined electrostatic potential. They used a shallow trench on the lower electrode, which formed an electrostatic trough in the plasma to confine the particles to 1-dimensional motion. Two particles, released in the trough appeared to have correlated motion corresponding to an attractive ion wakefield potential and a repulsive pair-wise interaction. In our computational approximation of Hebner's experiment, a metal washer placed on the lower electrode acts as a focus ring to warp the electric potential into a well to confine the dust particles. The motion of two particles having similar size as they settle in this potential well is shown in Fig. 5.11. On reaching the center of the well, the particle pair exhibits vertical oscillations before they settle in a stable configuration. The lower particle trapped in the ion-wake of the upper particle follows the upper particle as it moves up in the potential well. The plasma conditions at the final position lead to a larger particle charge for the upper particle and more repulsion and this leads to a larger interparticle separation.

The formation of a 3-D plasma crystal critically depends on the shape of the potential well and the manner of seeding of the dust particles. For example, we were able to obtain 3-D structures only by using a physically deep potential well and by seeding the

particles in this potential well with low initial speeds. Two-dimensional structures, similar to those obtained in the absence of the ion streaming force, can be obtained by having a physically wide and shallow potential well as shown in Fig. 5.12.

5.4 Conclusions

A self-consistent 3-D model has been developed to investigate the effect of ion streaming forces on Coulomb crystal formation in plasma processing reactors. On including the forces due to ion streaming, the plasma crystal has an amorphous structure that is dominated by vertical strings. We observe crystalline order in the vertical direction and an amorphous structure within a layer. Particles in lower layers exhibit more order. Particles form vertical-pairs and show correlated motion as they settle in the potential well. Ion streaming is found to play a significant role only for larger particle-sizes. The formation of a three-dimensional plasma crystal critically depends on the shape of the potential well and the manner of seeding of the dust particles.

5.5 Figures

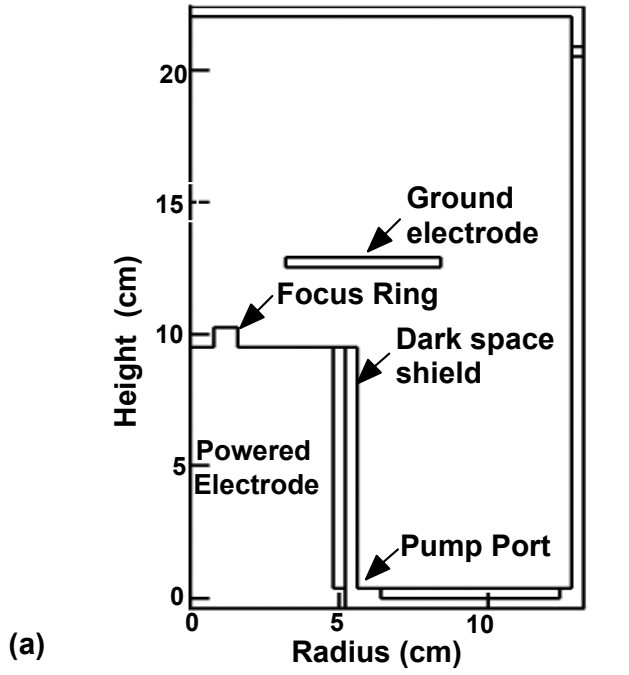

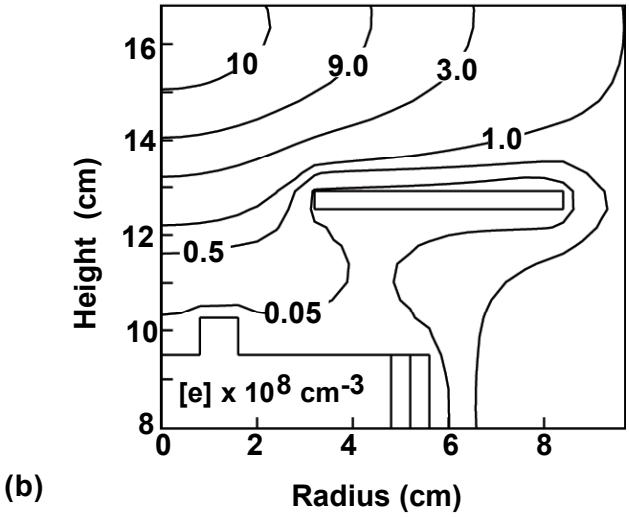

Fig. 5.1. Plasma properties in an Ar discharge (140 mTorr, 15 sccm, 1 W): (a) schematic of the modified GEC reference cell used in the simulations, and (b) electron density (10^8 cm^{-3}).

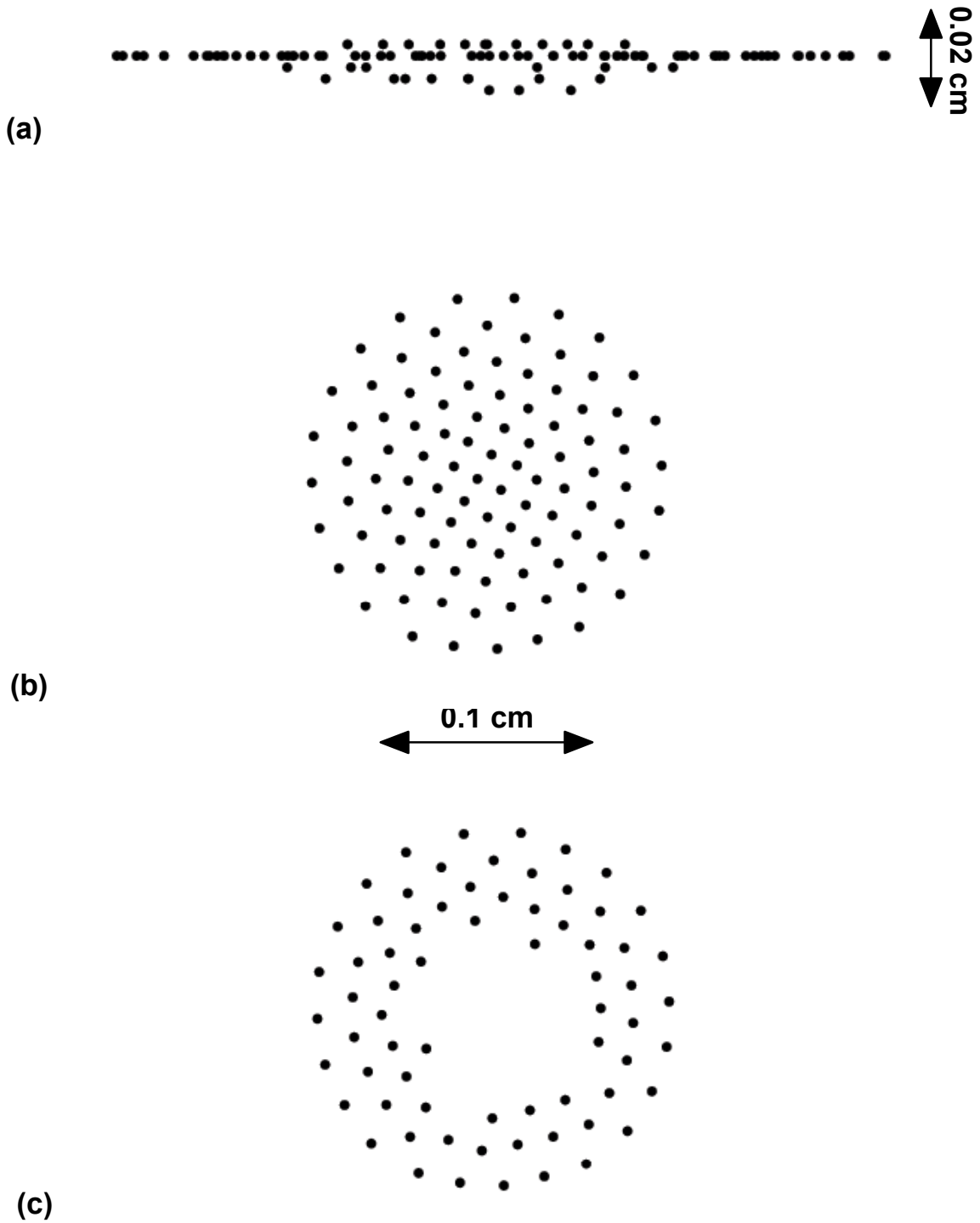

Fig. 5.2. Plasma crystal in an Ar discharge (140 mTorr, 15 sccm, 1 W, 100 1 μm particles) in the absence of ion streaming: (a) side view, (b) top view, and (c) top view of a single layer of particles.

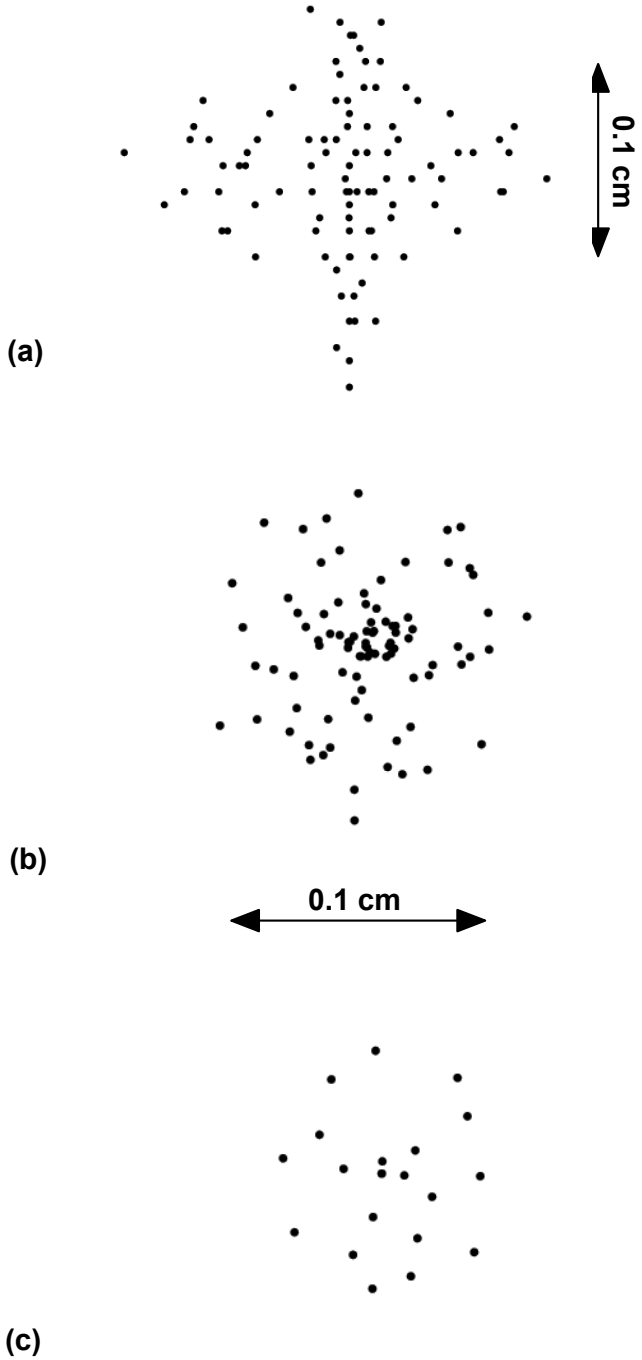

Fig. 5.3. Plasma crystal in an Ar discharge (140 mTorr, 15 sccm, 1 W, 100 1 μm particles) when ion streaming is included: (a) side view, (b) top view, and (c) top view of a single layer of particles.

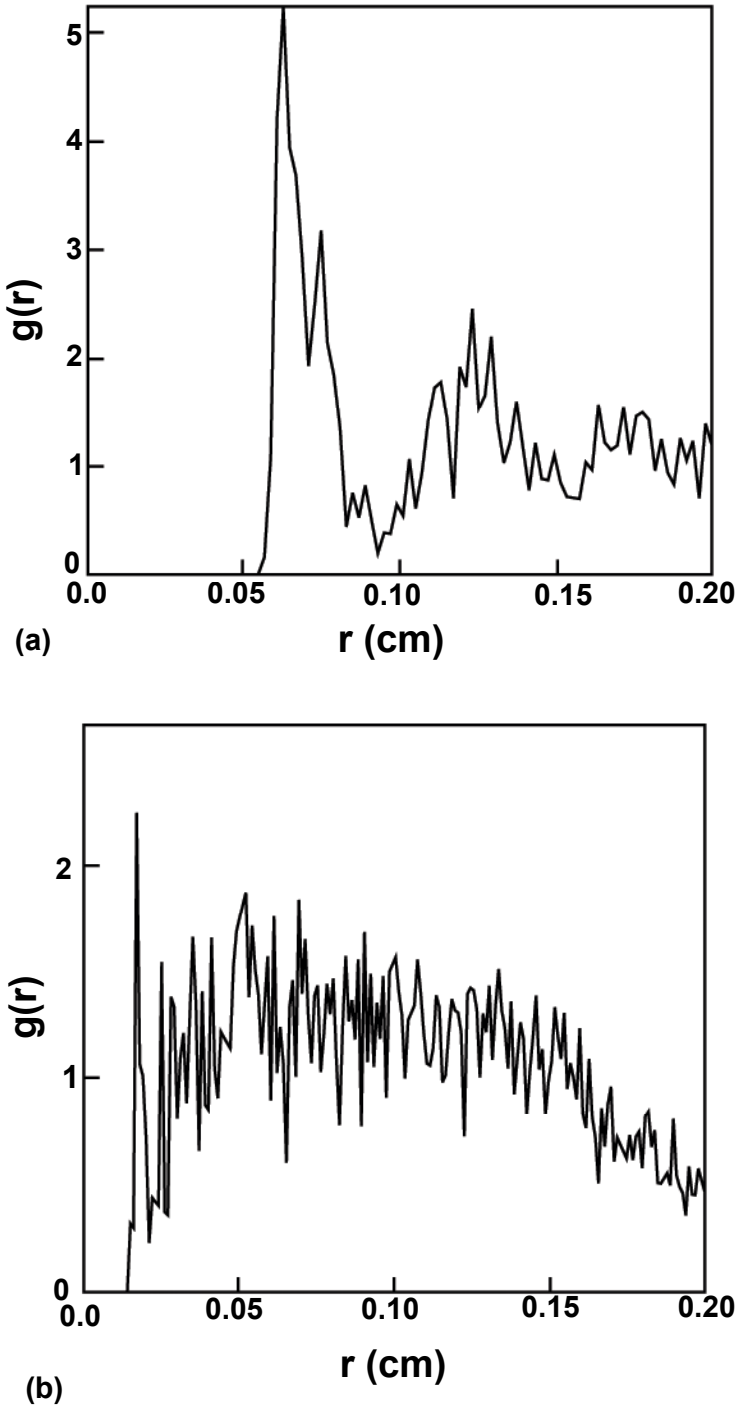

Fig. 5.4. PCF in an Ar discharge (140 mTorr, 15 sccm, 1 W, 1 μm particles): (a) *g(r)* indicates order in the absence of ion streaming force, and (b) *g(r)* has an amorphous structure indicating little order when ion streaming force is included.

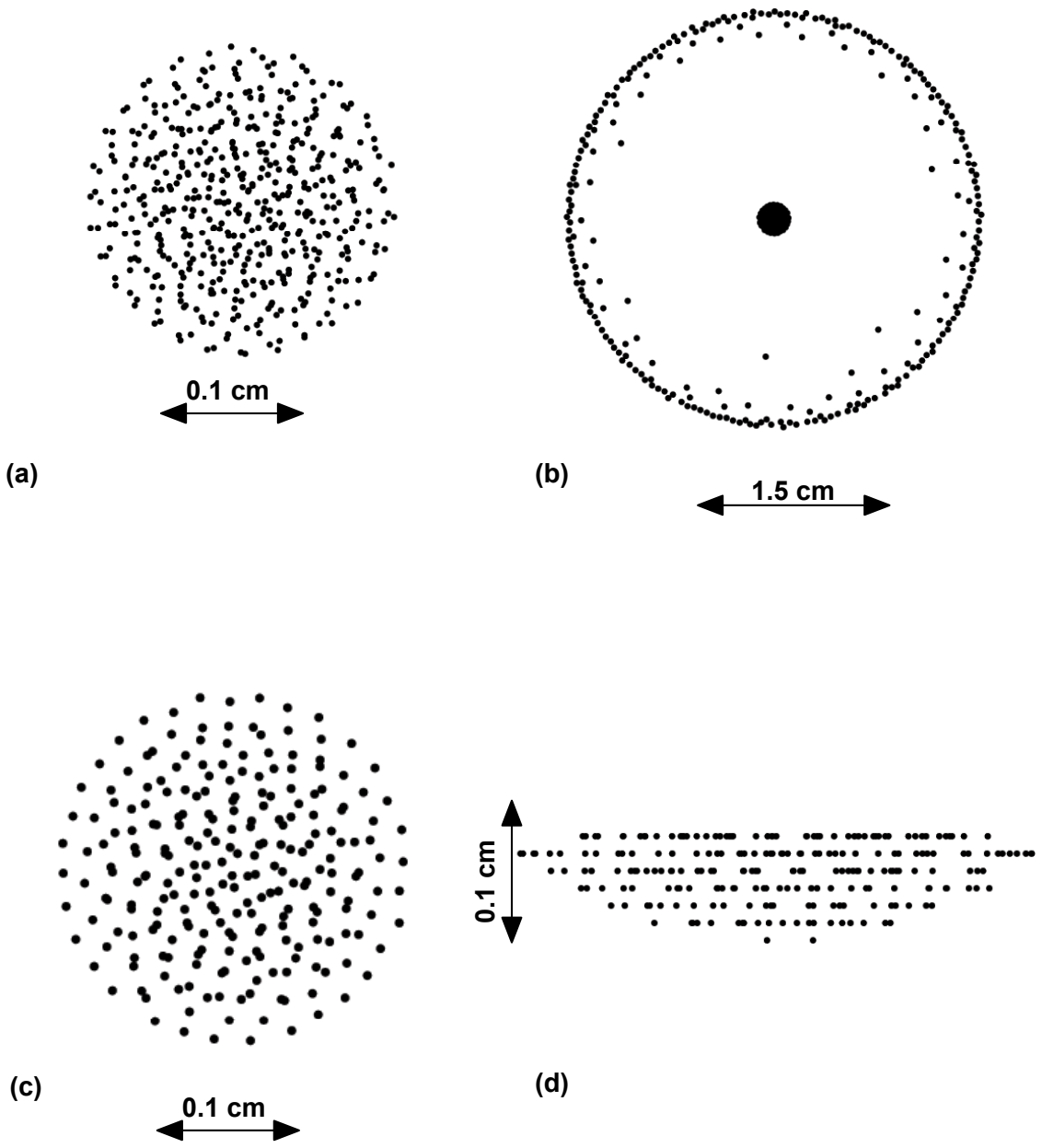

Fig. 5.5. Effect of increase in number of particles on the crystal morphology. Top view of the plasma crystal in an Ar discharge (140 mTorr, 15 sccm, 1 W, 400 1 μm particles) in the absence of ion streaming at different times: (a) 1s, (b) 10s, (c) after 30s ~ 250 particles remain in the reactor, and (d) side view after 30s.

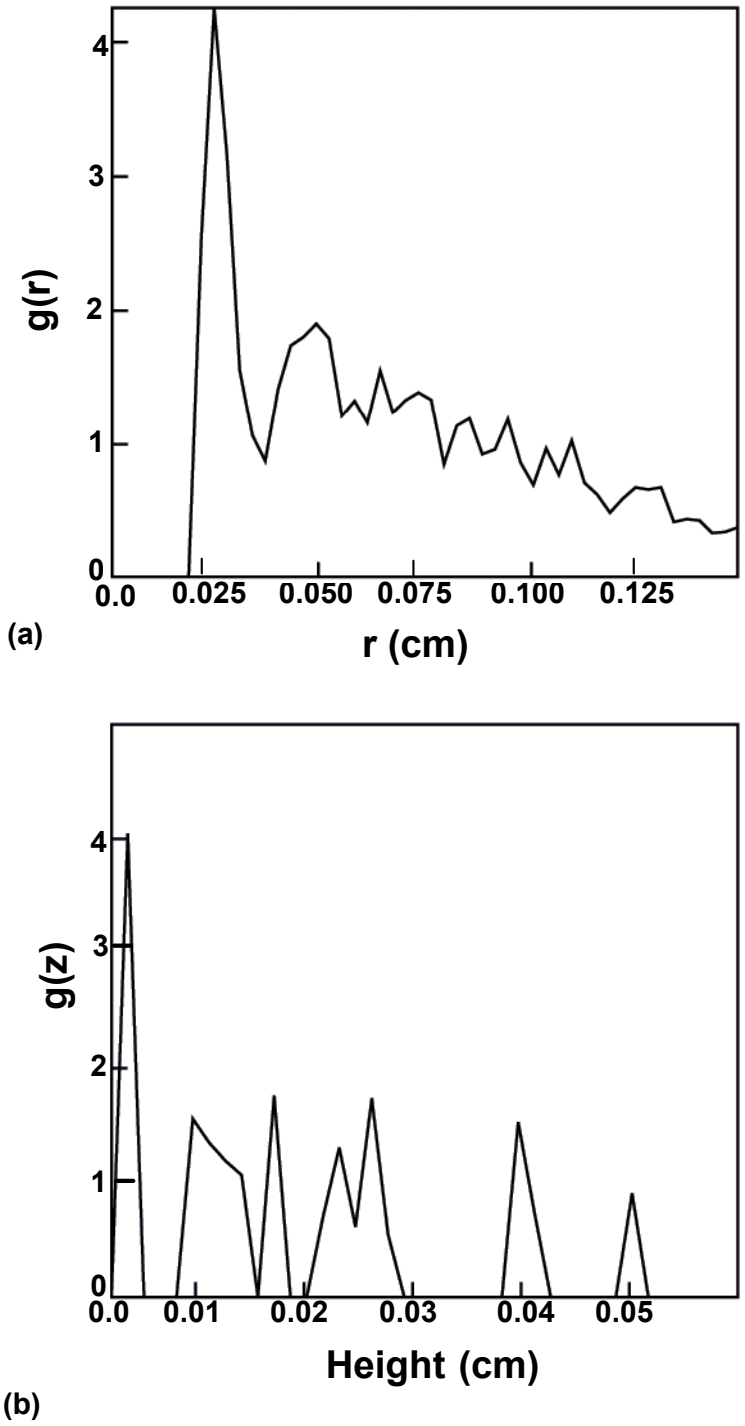

Fig. 5.6. PCF in an Ar discharge (140 mTorr, 15 sccm, 1 W, 400 1 μm particles) in the absence of ion streaming force: (a) *g(r)* indicates more order in the crystal on increasing the number of particles, and (b) *g(z)* indicates that the number of layers is small.

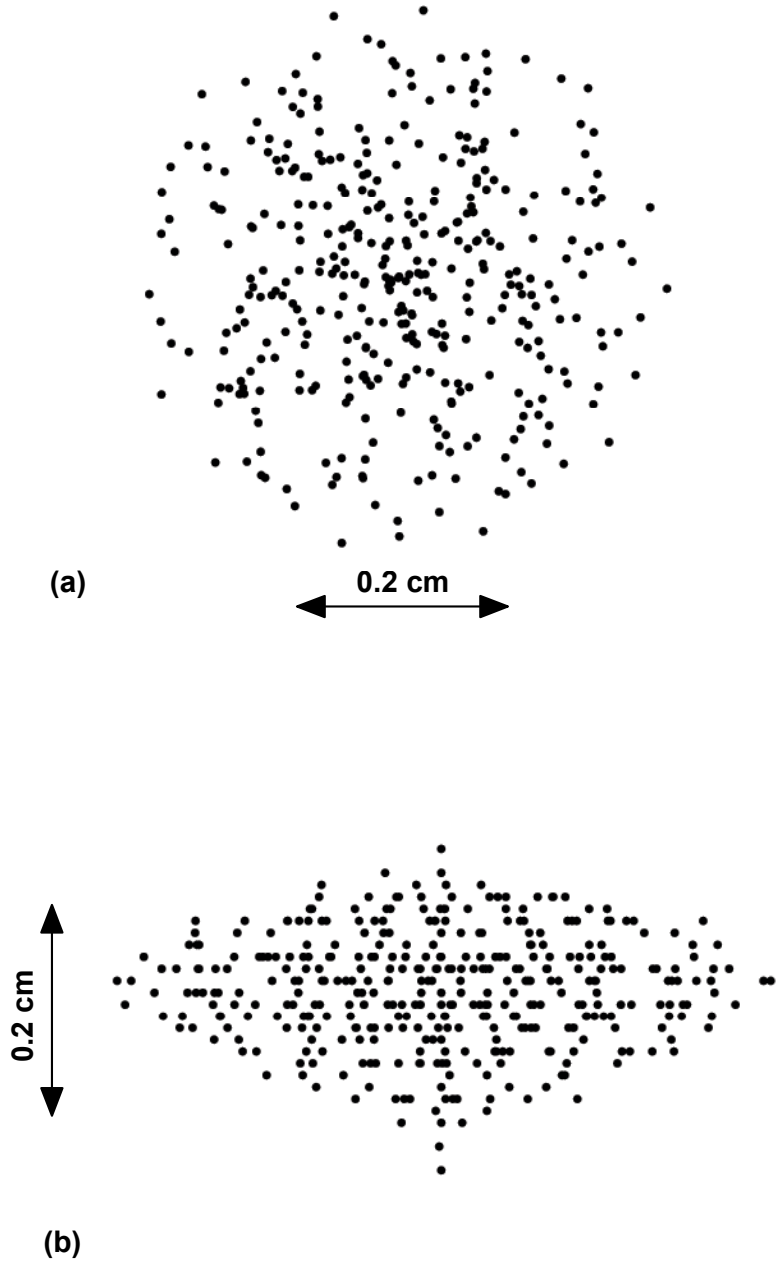

Fig. 5.7. Effect of increase in number of particles on the crystal morphology: (a) side view, and (b) top view of the plasma crystal in an Ar discharge (140 mTorr, 15 sccm, 1 W, 400 1 μm particles) when ion streaming force is included.

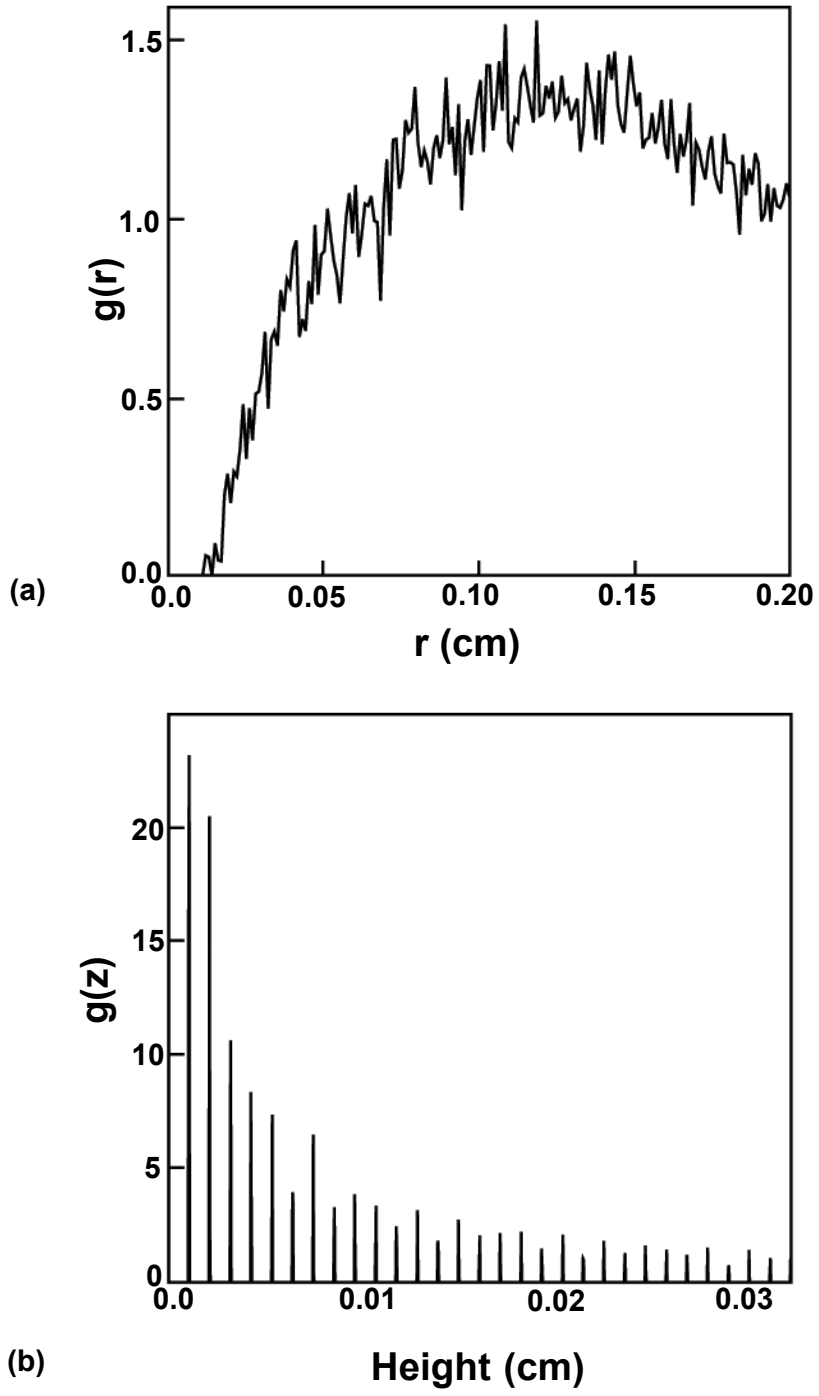

Fig. 5.8. PCF in an Ar discharge (140 mTorr, 15 sccm, 1 W, 400 1 μm particles) when ion streaming force is included: (a) within a layer, *g(r)* has an amorphous structure indicating little order, and (b) *g(z)* indicates order in the axial direction.

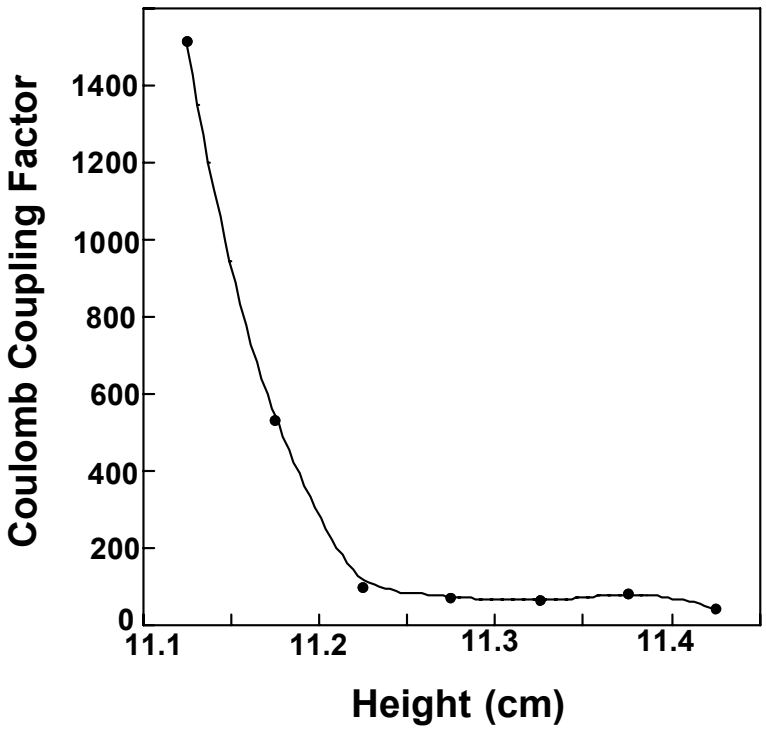

Fig. 5.9. Coulomb coupling factor as a function of height in the plasma crystal (140 mTorr, 15 sccm, 1 W, 400 1 μm particles). The layers lower in the crystal show more order.

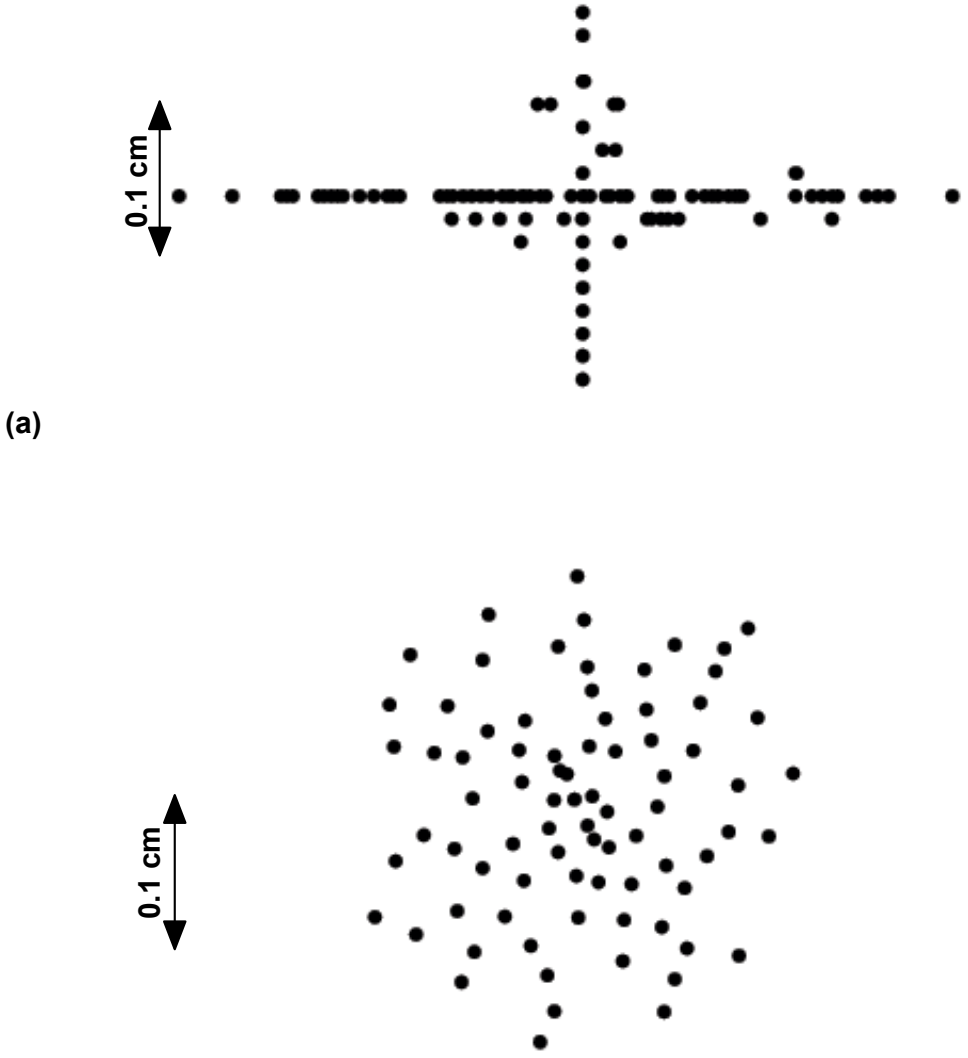

Fig. 5.10. Plasma crystal in an Ar discharge (140 mTorr, 15 sccm, 1 W, 100 0.1 μm particles) when ion streaming is included: (a) side view, and (b) top view. The 0.1 μm particles settle in far fewer layers than 1 μm particles. Ion streaming effects and consequently propensity to form 3-D structures is greater for larger particles.

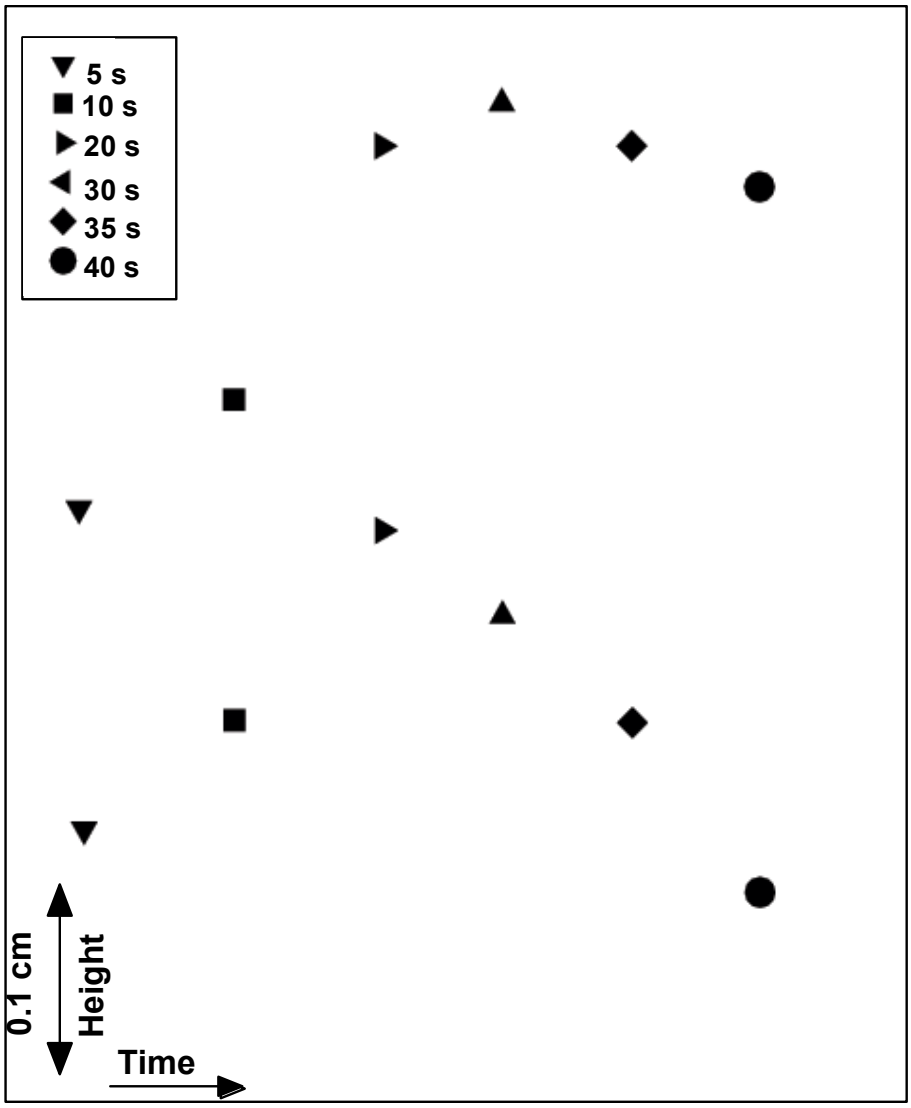

Fig. 5.11. Side view of the particle positions at different times as they settle in the potential well defined by the focus ring in an Ar discharge (140 mTorr, 15 sccm, 1 W). Particles with different sizes (1, 1.2 μm) form vertical-pairs and exhibit correlated motion.

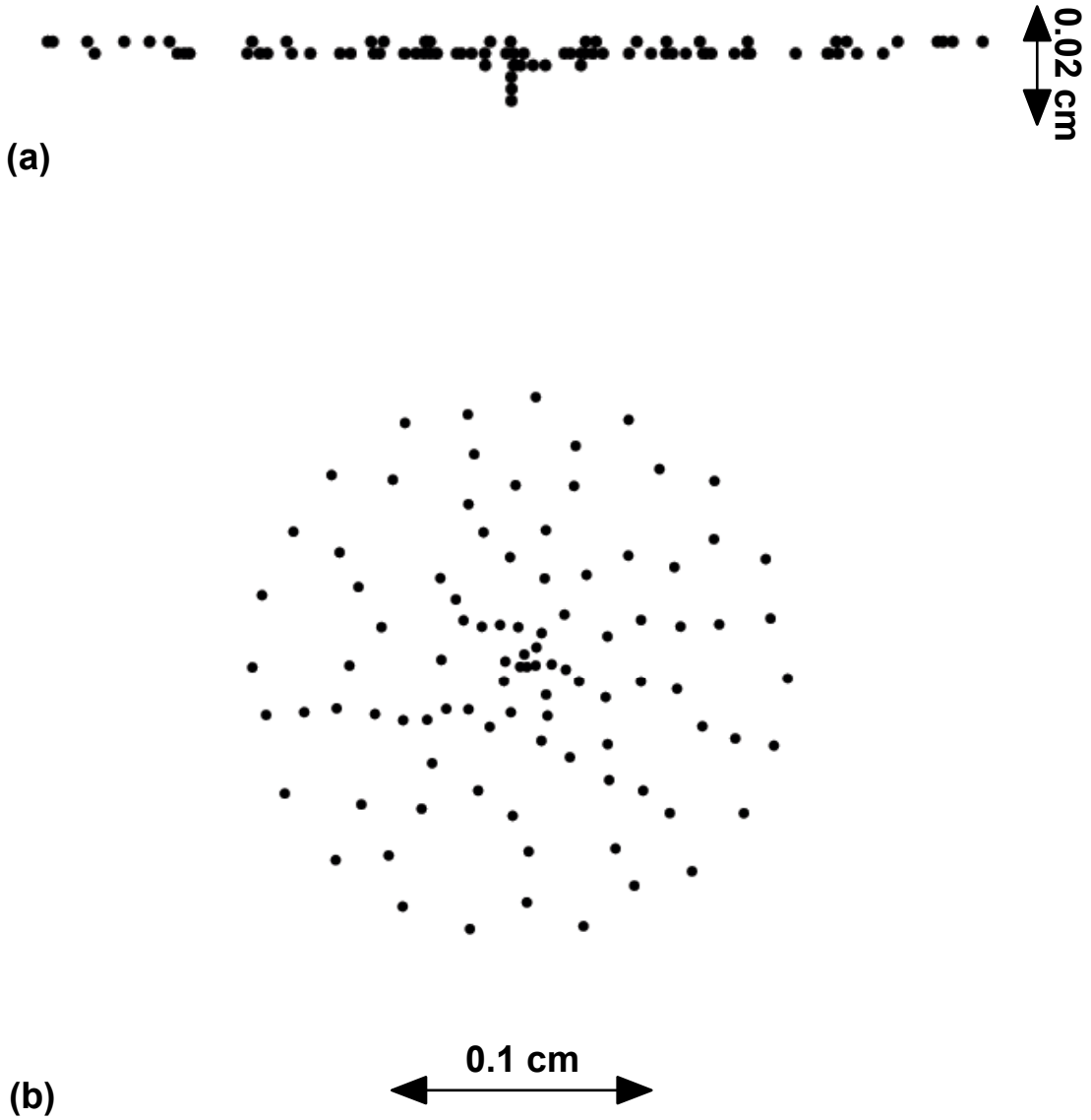

Fig. 5.12. Plasma crystal in an Ar discharge (140 mTorr, 15 sccm, 1 W, 100 1 μm particles) when ion streaming is included in a wide and shallow potential well: (a) side view, and (b) top view. 2-D structures similar to those obtained in the absence of the ion streaming force are observed.

5.6 References

[1] Y. Hayashi, Phys. Rev. Lett. **83**, 4764 (1999).

[2] M. Zuzic, et al. Phys. Rev. Lett. **85**, 4064 (2000).

[3] V. Steinberg, R. Sutterlin, A. V. Ivlev, and G. Morfill, Phys. Rev. Lett. **86**, 4540 (2001).

[4] S. V. Vladimirov and A. A. Samarian, Phys. Rev. E **65**, 046416 (2002).

[5] D. Samsonov, A. V. Ivlev, and G. E. Morfill, Phys. Rev. E **63**, 025401(R) (2001).

[6] G. A. Hebner, M. E. Riley, and B. M. Marder, Phys. Rev. E. (submitted for publication).

[7] M. Lampe, G. Joyce, and G. Ganguli, Phys. Plasmas **7**, 3851 (2000).

[8] S. A. Khrapak, A. V. Ivlev, and G. Morfill, Phys. Rev. E **64**, 046403 (2001).

[9] J. E. Hammerberg, D. S. Lemons, M. S. Murillo, and D. Winske, IEEE Trans. Plasma Sci. **29**, 247 (2001).

[10] M. Zuzic, A. V. Ivlev, J. Goree, G. E. Morfill, H. M. Thomas, H. Rothermel, U. Konopka, R. Sutterlin, and D. D. Goldbeck, Phys. Rev. Lett. **85**, 4064 (2000).

6. CONCLUSIONS

Dust particle transport in partially ionized plasmas has been the focus of many recent investigations as a consequence of concern over particle contamination of wafers during plasma processing of microelectronic devices and the use of particles to study nonideal plasmas. Under certain conditions such as low power, low pressure, moderate gas flows, and high particle density, Coulomb interactions between the dust particles dominate over the kinetic processes and the particles arrange in ordered lattices known as "Coulomb crystals." A self-consistent 3-D model has been developed to investigate particle transport and Coulomb crystal formation in plasma processing reactors. A dust particle transport model was integrated into a plasma equipment model to facilitate this study. The effect of varying the bias voltage of a capacitively coupled discharge, gas chemistries, particle diameter, and the number of particles on the propensity for crystal formation has been investigated.

At lower substrate bias, a single disk-shaped lattice of dust particles is obtained, which is confined to the center of the potential well. In the center of the lattice where the confining forces (which are largely electrostatic and gravitational compressive forces from particles at larger radii) are largest, the lattice has regular hexagonal structure. As the bias is increased, the larger ion drag force pushes the particles out into an annular lattice and a void forms in the center of the crystal. These ringlike structures collapsed to a disk upon addition of electronegative gases, commensurate with a shift in the net ion momentum flux vectors to having a radially inward component.

The interparticle spacing decreases on increasing the number of particles in the lattice due to larger compressive forces from particles at larger radii. The nearest neighbor spacing is smallest in the center of the crystal where the compressive forces of particles at larger radii is the largest. As one moves to larger radii, the compressive forces due to outlying particles lessens, leaving only the plasma confining forces, producing a larger interparticle separation. As dust particles settle into the potential well forming a Coulomb solid, the resulting lattice often oscillates about an equilibrium position. These radial and horizontal oscillations are the result, in part, of the mutual repulsion of the particles in the presence of a restoring force, in this case both gravity and electrostatic plasma forces.

On including the forces due to ion streaming, the plasma crystal has an amorphous structure that is dominated by vertical strings. There is crystalline order in the vertical direction and an amorphous structure within a layer. In 3-D plasma crystals, particles in lower layers exhibit more order. Particles form vertical-pairs and show correlated motion as they settle in the potential well. Ion streaming plays a significant role only for larger particle-sizes. The formation of a 3-D plasma crystal critically depends on the shape of the electrostatic potential well and the manner of seeding of the dust particles.